MULTISCALE MODEL. SIMUL.
Vol. 15, No. 4, pp. 1768–1796

A MICRO-MACRO FRAMEWORK FOR ANALYZING STERIC AND HYDRODYNAMIC INTERACTIONS IN GLIDING ASSAYS*

STEVEN C. COOK†, CHRISTEL HOHENEGGER‡, AND TAMAR SHINAR†

Abstract. Macroscopic flows of filament-motor mixtures, driven by the hydrolysis of ATP, are important to many cellular processes such as cytoplasmic streaming in *Drosophila* oocytes and cortical flow in the first cell division of *C. elegans*. Gliding assays, reduced in vitro model systems where motor proteins adsorbed onto a planar substrate bind to and move filaments, recreate large-scale dynamic patterns like coherent swarming motion and density waves. These systems are sensitive to the microscopic behavior such as motor protein binding and unbinding dynamics, which take place on a faster timescale than the direct and fluid-mediated filament interactions. In this work, we present a multiscale modeling and simulation framework for gliding assays that allows detailed microscopic motor modeling as well as both steric and hydrodynamic interactions between filaments. Our model is based on continuum kinetic theory, and our implementation utilizes CPU and GPU parallelism to track the sparse but high-dimensional state space arising from the microscopic motor protein configurations. We find that steric interactions play a role in the formation of spatiotemporally coherent flow structures and qualitatively reproduce experimentally observed behaviors including filament crossover and alignment and clump formation, merging, and splitting.

Key words. micro-macro methods, multiscale simulation, gliding assay, cytoskeleton, motor proteins, active suspensions, hydrodynamics, solid-fluid coupling, steric interactions, heterogeneous computing, emergent phenomena

AMS subject classifications. 76Z99, 76M20, 76M22, 92C05, 65C20, 68U20, 65Y05

DOI. 10.1137/17M1113503

1. Introduction.

Actin and tubulin filaments working in concert with motor proteins play a central role in cell functions including mitosis and pronuclear centering [32]. Gliding assays, in which stabilized filaments are propelled by anchored motor proteins powered by the hydrolysis of ATP in a thin quasi–two-dimensional chamber, are commonly used to study the behavior of these cellular components in vitro (see Figure 1). Large-scale pattern formation is observed in such experiments, including clump formation, merging, splitting, density waves [30], and the emergence of a lattice of microtubule vortices [33].

The physics of the filament-motor-fluid system are inherently multiscale in space and time, with nanoscale motors with fast binding/unbinding kinetics coupled to microscale filaments interacting in a macroscopic fluid domain. These systems have been studied with a variety of theoretical and computational approaches. Models that track explicit representations of filaments with Langevin dynamics underscore the sensitivity of the system to the motor behavior; [15, 16] included a load-dependent force-velocity relationship of motor proteins in a gliding assay and found that the motor activity

*Received by the editors January 30, 2017; accepted for publication (in revised form) September 27, 2017; published electronically December 6, 2017.
http://www.siam.org/journals/mms/15-4/M111350.html
Funding: The work of the first and third authors was partially supported by the National Institute of General Medical Sciences of the National Institutes of Health under award R01GM104976. The content is solely the responsibility of the authors and does not necessarily represent the official views of the National Institutes of Health. The third author's work was also supported by the Amrik Singh Poonian endowed chair at the University of California, Riverside.

†Department of Computer Science, UC Riverside, Riverside, CA 92521 (scook005@cs.ucr.edu, shinar@cs.ucr.edu).
‡Department of Mathematics, University of Utah, Salt Lake City, UT 84112 (choheneg@math.utah.edu).

increases nematic ordering, and [20, 21, 23] found that the time spent by individual motors at the end of a microtubule before falling off plays a central role in the emergence of coherent structures. These models neglect fluid-mediated filament-filament interactions and are therefore not suitable for addressing such behaviors. Moreover, the computations have scaled to only hundreds of filaments, while many systems of interest such as the mitotic spindle are estimated to have tens or hundreds of thousands of filaments. A model based on macroscopic configuration fields, and thus more suitable to a large system and large length and time scales, was proposed by [17]. This was expanded upon by [28] in a hydrodynamic theory incorporating explicit tracking of bound and unbound motor populations. Both [17] and [28] rely on phenomenologically motivated constitutive equations in the model derivation and neglect filament density fluctuations. Another class of modeling approaches starts with a microscopic model and coarse-grains the system to attain a macroscopic description [1, 19, 34]. For example, [19] assumes a constant motor density and demonstrates that inhomogeneities in motor stepping rate are necessary to drive bundle formations, and [34], without considering fluctuations in motors or filament densities, shows that the order of the isotropic-nematic transition depends on the force-dependent motor detachment. However, [1, 34] neglect fluid-mediated filament-filament interactions, although they could be coupled to the fluid equation using a configurational average of an expression involving the distribution function to include the contribution of the particles to the fluid stress [4, 5]. This approach has been widely applied to nanorods [35], and more recently to active gels [18] and to suspensions of active swimmers [26, 27], and was used in our previous work [12]. Such methods have the benefit of flexibly allowing detailed microscopic modeling. However, it is not always possible to avoid tracking the microscopic variables, which can incur significant computational cost.

As shown experimentally by, among others, [15, 30, 33], the filament density and steric interactions play a critical role in the formation of coherent structures. In this paper we consider dense suspensions of filaments, and we build upon our previous model [12] to include steric interactions between filaments. A widespread model of steric interaction is the excluded volume potential [5]. This model, widely used in liquid crystal theory [19, 35], has been adapted to active suspensions of self-propelled pushers and pullers in three dimensions [8]. The latter includes a rotational steric alignment term but neglects the linear steric contribution, which can prevent unphysical "piling up" amongst the microtubules in a gliding assay. We broaden this approach to modeling steric interactions, including both rotational and linear steric interaction terms.

Characterizing the interplay of steric versus hydrodynamic effects requires an exploration of different filament densities and motor systems. At a microtubule density of $.05\mu\text{m}^{-2}$, Sumino et al. [33] are able to model their experimentally observed vortex lattice with a phenomenological agent-based method neglecting hydrodynamics. In contrast, at actomyosin surface densities ranging between $2\mu\text{m}^{-2}$ and $21\mu\text{m}^{-2}$, Schaller et al. [30] demonstrate filament clump and density wave persistence and scale that cannot be explained through purely steric interactions. Additionally, Schaller et al. [29] demonstrate evidence of hydrodynamic effects in the formation of depletion layers between clump-clump or clump-wall collisions that cause reorientation before physical contact. The particulars of the microscopic motors may also significantly influence the collective motion. For example, [33] reports that using kinesin motor proteins instead of dynein results in a higher rate of microtubule crossover events, limiting steric interactions and preventing the formation of a vortex lattice. The importance of fluid effects can also be seen further in the theoretical study of filaments in a quasi–two-dimensional chamber [11].

In this work, we present a novel micro-macro model and computational framework to simulate both steric and hydrodynamic interactions in a microtubule gliding assay. Our new framework supports different motor protein activity models, as well as the option to treat the filaments as self-propelled. Rather than use phenomenological steric interaction rules, we model fluid stresses due to microtubule inextensibility, rotational and translational steric interactions, and self-propulsion if applicable.

We base our approach on our previous work [12], where we developed a continuum model coupling the motion of the fluid to the motion of the motors and microtubules. In that work, we used closure approximations to reduce the fluid equations to depth-averaged two-dimensional equations, and restricted ourselves to the dilute limit, ignoring steric interactions. Here, we solve the fluid equations in three dimensions and avoid making closure approximations. As in [12], we track distributions of microtubules and kinesin motor proteins, with behavior governed by conservation equations.

The paper is organized as follows: Our framework is presented in section 2, the implementation and numerical methods are presented in section 3, simulation results are presented in section 4, and we conclude in section 5.

2. Modeling framework. This section reviews the setup of a gliding motility assay, describes our continuous representation, and details the individual components of our modeling framework. Two distributions are tracked: one for the microtubules and one for the bound motors. Each distribution satisfies a conservation equation. We present one such equation for the microtubule distribution, taking into account hydrodynamic and steric effects, and two for the bound motor distribution. Bulk fluid forces and steric stresses are calculated from the bound motor proteins and the microtubule distribution, respectively, and are included in the fluid equations.

2.1. Microscale model. Figure 1 illustrates the experimental setup. A microtubule gliding assay consists of two plates separated by a small distance. A fluid fills the gap, with fluid flow characterized by low Reynolds number. Motor proteins (kinesin in our case) are anchored to the bottom plate with their heads free to bind to microtubules, walk along them, and detach. The microtubules, in turn, glide along the motor protein heads, effectively constrained within a single plane. They are stabilized to prevent growth or depolymerization, and have an orientation defined in terms of a plus and minus end. Upon binding, kinesin motor proteins walk towards the plus end of the microtubule, propelling the microtubule in the direction of its minus end. We assume ATP saturation, so the motor proteins are continuously active. We refer the reader to [12] for a list of values of physical parameters found in the literature.

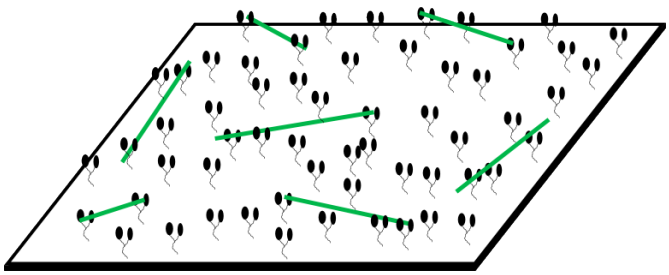

FIG. 1. *Microtubule gliding assay setup. Motor protein (black) tails are anchored to a fixed plate, while their heads bind and pull microtubules (green). (See online version for color.)*

2.1.1. Microtubule distribution. In this model, we assume that the microtubules of length $2l$ and diameter b are inextensible and rigid, an appropriate approximation for microtubules of $l \leq 2\mu$m [31]. We describe the microtubules by the position of their center-of-mass $\mathbf{x}$ and a vector $\mathbf{p}$ pointed towards their plus end. Let $\Psi(\mathbf{x}, \mathbf{p}, t)$ be the microtubule distribution function. Ψ evolves according to the Smoluchowski equation (see also [12, 13])

$$\partial_t \Psi + \nabla_x \cdot (\dot{\mathbf{x}}\Psi) + \nabla_p \cdot (\dot{\mathbf{p}}\Psi) = 0, \tag{1}$$

$$\dot{\mathbf{x}}_2 = -V_{\mathrm{sp}}\mathbf{p}_2 + \mathbf{u}_2(\mathbf{x}) - \nabla_{x_2} U_t - D_{\mathrm{t},||}\nabla_{x_2} \ln \Psi, \tag{2}$$

$$\dot{z} = w(\mathbf{x}) - \partial_z U_t - D_{\mathrm{t},\perp}\partial_z \ln \Psi, \tag{3}$$

$$\dot{\mathbf{p}} = (\mathbf{I} - \mathbf{pp})\nabla_x \mathbf{u}(\mathbf{x})\mathbf{p} - \nabla_p U_r - D_{\mathrm{r}}\nabla_p \ln \Psi. \tag{4}$$

Here the subscript 2 denotes the in-plane x, y components and derivatives with respect to these variables. The first two and last terms in the equations for $\dot{\mathbf{x}} = (\dot{\mathbf{x}}_2\ \dot{z})^T$ and $\dot{\mathbf{p}}$ are similar to those of the active bacteria swimming model of [27]. V_{sp} is a propulsion speed, analogous to the self-propulsion term in active swimmer models. In our model, motor forces spread to the fluid grid (described below) can only be resolved on the scale of the fluid grid. We allow a phenomenological self-propulsion velocity to compensate for this reduction in resolution of microtubule motion. Since microtubules do not propel themselves through the fluid as a bacterium does [29], but are propelled by motors, the resulting force should act like a monopole (see (15)–(16)), similar to sedimenting particles [6]. Therefore, we include both a self-propulsion velocity and a passive force in our model. Furthermore, $\mathbf{u}(\mathbf{x}) = (\mathbf{u}_2(\mathbf{x})\, w(\mathbf{x}))^T$ is the velocity of the surrounding fluid at $\mathbf{x}$ with which the microtubules are advected. Because the kinesin motors walk towards the plus end, i.e., in the direction of $\mathbf{p}$, the microtubule will move in the direction $-\mathbf{p}_2$ in the plane of motion where it is restricted to leading order, as shown in [12]. $D_{\mathrm{t},||}$, $D_{\mathrm{t},\perp}$ and D_{r} are the translational and rotational diffusion coefficients, respectively. Because of the channel geometry and the experimental observation that microtubules move in a z-plane, we expect $D_{\mathrm{t},\perp}$, the diffusion in the z direction, to be smaller than the in-plane diffusion, $D_{\mathrm{t},||}$. We use zero diffusion in all of our examples. We also do not include thermal fluctuations in the present model. The third term in $\dot{\mathbf{x}}_2$ and $\dot{\mathbf{p}}$ and the second term in $\dot{z}$ describe the effect of steric interactions through a translational and rotational potential, $U_{t/r}$, respectively. We model the steric potential using the Maier–Saupe potential $K_{t/r}(\mathbf{p}, \mathbf{p}') = -U^0_{t/r}(\mathbf{p} \cdot \mathbf{p}')^2$ with

$$U_{t/r}(\mathbf{x}, \mathbf{p}, t) = \int \Psi(\mathbf{x}, \mathbf{p}', t) K_{t/r}(\mathbf{p}, \mathbf{p}') d\mathbf{p}'.$$

The above form of U_r is identical to that proposed by [8] for active suspension, but we also keep the translational steric potential U_t from [2, 19] to prevent interpenetration in the plane of the microtubules. Neglecting this term was less consequential for [8], as their model is three-dimensional; our two-dimensional rod reduction below (section 2.2) leads to a more highly constrained geometry in which this term is important. With this term included, we see behavior closer to the experiments of Schaller et al. [29], where clumps grow in extent rather than increasingly concentrating into a small area. We refer the reader to [2] for details on how the translational term arises in the Smoluchowski equation for the microtubule density. With the previous definitions of

the steric potential, the translational and rotational fluxes become

$$\dot{\mathbf{x}}_2 = -V_{\mathrm{sp}}\mathbf{p}_2 + \mathbf{u}_2(\mathbf{x}) + U^0_{t,\parallel}\mathbf{pp} : \nabla_2\mathbf{D}(\mathbf{x},t) - D_{\mathrm{t},||}\nabla_2 \ln\Psi, \tag{5}$$

$$\dot{z} = w(\mathbf{x}) + U^0_{t,\perp}\mathbf{pp} : \partial_z\mathbf{D}(\mathbf{x},t) - D_{\mathrm{t},\perp}\partial_z \ln\Psi, \tag{6}$$

$$\dot{\mathbf{p}} = (\mathbf{I}-\mathbf{pp})(\nabla_x\mathbf{u}(\mathbf{x}) + 2U^0_r\mathbf{D}(\mathbf{x},t))\mathbf{p} - D_{\mathrm{r}}\nabla_p \ln\Psi, \tag{7}$$

where $\mathbf{D}(\mathbf{x},t) = \int \Psi(\mathbf{x},\mathbf{p},t)\mathbf{pp}d\mathbf{p}$ is the second moment of Ψ with respect to $\mathbf{p}$. The total number of microtubules is given by $N = \iint \Psi d\mathbf{x}d\mathbf{p}$.

2.1.2. Motor distributions. In general, the free and bound motor populations evolve according to a reaction-diffusion-advection equation. In a gliding assay, motor tails are fixed to a plate and cannot diffuse or advect with the flow. Hence, we consider only the conversion between the free and bound populations, and the advection and procession of the bound motor heads. We represent the free motor density as $\mathcal{M}_f(\mathbf{r}_0)$, the density of motors with free heads and tails anchored at position $\mathbf{r}_0$. We do not track the position of free motor heads. We represent the bound motor density per microtubule as $\mathcal{M}_b(\mathbf{r}_0, s|(\mathbf{x},\mathbf{p}),t)$, with $\mathbf{r}_0$ the position where the motor tail is anchored, $\mathbf{x}, s, \mathbf{p}$ the center of mass, arclength parameter, and orientation of the microtubule the motor head is bound to, and t the time. The notation $|(\mathbf{x},\mathbf{p})$ denotes that the probability is conditional on the distribution of microtubules $\Psi(\mathbf{x},\mathbf{p},t)$. Finally, we let $\mathcal{M}(\mathbf{r}_0)$ be the total (bound + free) motor density at $\mathbf{r}_0$. We define the free motor density $\mathcal{M}_f$ as

$$\mathcal{M}_f(\mathbf{r}_0,t) = \mathcal{M}(\mathbf{r}_0) - \iiint \mathcal{M}_b(\mathbf{r}_0, s|(\mathbf{x},\mathbf{p}),t)\Psi(\mathbf{x},\mathbf{p},t)ds\, d\mathbf{x}\, d\mathbf{p}; \tag{8}$$

that is, for every motor with tail anchored at $\mathbf{r}_0$ the head is either free or bound. The total number of bound motors is given by $N_b = \iiiint \mathcal{M}_b\Psi d\mathbf{r}_0 d\mathbf{x} d\mathbf{p} ds$. In the entire system, the total number of motors $N_m = N_f + N_b$ is constant.

The possible configurations of bound motor heads face constraints. First, a head detaches if it walks off the plus end of the microtubule ($|s| > l$). Second, the motor head detaches due to stretching of the motor stalk, which happens beyond a critical distance r_c. We do not model the spring force of the motor stalk extension. We enforce these two constraints by requiring that $\mathcal{M}_b$ be zero when $|s| > l$ and by taking $\mathcal{M}_b$ to be zero when $|\mathbf{x} + s\mathbf{p} - \mathbf{r}_0| \geq r_c$. Equivalently, the second condition says that for a given tail $\mathbf{r}_0$ there is only a small subset of $\mathbf{x} + s\mathbf{p}$ available for attachment. This crucial locality restriction effectively reduces the dimensionality of $\mathcal{M}_b$. We represent the allowable local configurations as a ball of radius r_c (illustrated in Figure 2),

$$B_{r_c}(\mathbf{r}_0) = \{(\mathbf{x}', s', \mathbf{p}') : |\mathbf{x}' + s'\mathbf{p}' - \mathbf{r_0}| < r_c\}. \tag{9}$$

We consider two equations for the bound motor distribution. The first, hereafter referred to as the "evolved" model, tracks $\mathcal{M}_b$ through the evolution of a full conservation equation. It models motor head stepping along microtubules as well as attachment proportional to the available number and length of microtubules and detachment. Since motors bind and unbind quickly relative to the speed of the microtubules, this conservation equation has its own smaller timescale. The second model, hereafter referred to as the "simplified" model, assumes that motors bind to any reachable position s along a microtubule with equal probability, and that the distribution of bound motors $\mathcal{M}_b\Psi$ with tails anchored at $\mathbf{r}_0$ is proportional to the density of microtubules to bind to up until all available motors are bound. The fidelity

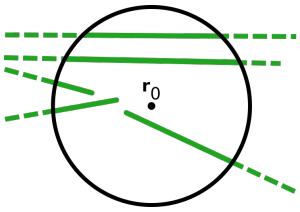

FIG. 2. *Set $B_{r_c}(\mathbf{r}_0)$ of microtubule segments accessible to motor head for motor tail anchored at $\mathbf{r}_0$ in solid green (illustrated in two dimensions for clarity).*

of the smaller timescale behavior from the evolved motor model is lost. Instead of solving a conservation equation at a separate timescale, $\mathcal{M}_b$ is updated from Ψ on its own timescale.

In the evolved motor model, following [22], the number of binding events per second is proportional to the local density of free motors times the available length of microtubules (as an approximation for the available binding sites) with the constant of proportionality, denoted by $\overline{k_{\text{on}}}$, that has units of $\mu\text{m}^2\text{s}^{-1}$. Defining $\bar{B}(\mathbf{r}_0) = \iiint_{B_{r_c}} \Psi \mathcal{M}_b ds d\mathbf{x} d\mathbf{p}$, then $\bar{B}(\mathbf{r}_0)$ represents the number of bound motors in B_{r_c} per unit area. Since $\bar{B}$ and $\mathcal{M}_f$ have units of number per unit area (and not per unit volume), we divide $\overline{k_{\text{on}}}$ by the capture radius r_c to obtain a constant of proportionality that has units of $\mu\text{m s}^{-1}$, before repeating the argument of [22] for $\bar{B}$. In order to convert from a number per area to a number, we multiply $\bar{B}(\mathbf{r}_0)$by the area of the disk D_{r_c} of radius r_c centered at $\mathbf{r}_0$. Therefore, after dividing through by $|D_{r_c}|$ and neglecting advection terms, we have a relationship of the form

$$\partial_t \bar{B} = -k_{\text{off}} \bar{B} + \frac{\overline{k_{\text{on}}}}{r_c |D_{r_c}|} \mathcal{M}_f \iiint_{B_{r_c}} \Psi d\mathbf{x} d\mathbf{p} ds,$$

where the integral of Ψ over B_{r_c} represents the total length of available microtubules and where k_{off} (units of s^{-1}) is the detachment rate. Setting $k_{\text{on}} = \overline{k_{\text{on}}}/(r_c|D_{r_c}|)$ with units of $(\mu\text{ms})^{-1}$ and including advection terms, the conservation equation for $\mathcal{M}_b\Psi$ is

$$\begin{aligned} \partial_t(\mathcal{M}_b\Psi) + \partial_s(V_{\text{m}}\mathcal{M}_b\Psi) + \nabla_x \cdot (\dot{\mathbf{x}}\mathcal{M}_b\Psi) + \nabla_p \cdot (\dot{\mathbf{p}}\mathcal{M}_b\Psi) \\ = k_{\text{on}}\Psi\mathcal{M}_{\text{f}}\mathbb{1}_{B_{r_c}(\mathbf{r}_0)} - k_{\text{off}}\mathcal{M}_b\Psi. \end{aligned} \tag{10}$$

Here $\mathbb{1}_{B_{r_c}}(\mathbf{r}_0)$ is the indicator function for $B_{r_c}(\mathbf{r}_0)$. The flux terms on the left-hand side express the procession of the motor along the microtubule with speed V_{m} and the motion of the motor-microtubule complex with the background flow. The source terms on the right-hand side express the attachment of a free motor at s to the microtubule $\mathbf{x}, \mathbf{p}$ at a rate per length k_{on}, and the detachment of a bound motor at a rate k_{off}. Using (1) to eliminate Ψ, (10) simplifies to

$$\left[\partial_t \mathcal{M}_b + \partial_s(V_{\text{m}}\mathcal{M}_b) + \dot{\mathbf{x}} \cdot \nabla_x \mathcal{M}_b + \dot{\mathbf{p}} \cdot \nabla_p \mathcal{M}_b\right] \Psi = k_{\text{on}}\mathcal{M}_f \Psi \mathbb{1}_{B_{r_c}} - k_{\text{off}}\mathcal{M}_b\Psi. \tag{11}$$

We note that if $\Psi \neq 0$ for all $(\mathbf{x}, \mathbf{p}, t)$, we can divide by Ψ, but we will refrain from doing so until section 2.2.

In this paper, we also consider a simplified heuristic motor model where all motor heads are located in the same plane at height z_0 and the number of bound motors is proportional to the number of microtubules available within the binding range.

Therefore, we let $\mathcal{M}_b$ be the piecewise function

$$\mathcal{M}_b(\mathbf{r}_0, s|(\mathbf{x},\mathbf{p}),t) = \begin{cases} 0 & \text{if } |\mathbf{x}+s\mathbf{p}-\mathbf{r}_0| \geq r_c, \\ \min\left(C, \frac{\mathcal{M}(\mathbf{r}_0)}{\iiint_{B_{r_c}} \Psi d\mathbf{x} d\mathbf{p} ds}\right) & \text{if } |\mathbf{x}+s\mathbf{p}-\mathbf{r}_0| < r_c. \end{cases} \tag{12}$$

In the above, the cutoff constant C has the same units as $\mathcal{M}_b$. The second term in the minimum effectively caps $\mathcal{M}_b$ so that $\iiint_{B_{r_c}} \mathcal{M}_b \Psi d\mathbf{x} ds d\mathbf{p} \leq \mathcal{M}$, the total available motors at $\mathbf{r}_0$. Above the threshold value C, all local motor heads are bound. As C increases, so do the number of bound motors at $\mathbf{r}_0$ for a fixed value of $\iiint_{B_{r_c}} \Psi d\mathbf{x} ds d\mathbf{p}$, so larger C values decrease the minimum rod density needed to bind all local motors.

2.1.3. Fluid. The bulk fluid motion is described by the incompressible Stokes equations for low Reynolds number flows with suspended microtubule and motor microstructure. As is customary [3], the total stress in the fluid can be divided into a Newtonian stress and an extra stress arising from the microstructure, leading to

$$-\mu \nabla^2_{\mathbf{x}} \mathbf{u}(\mathbf{x}) + \nabla_{\mathbf{x}} q(\mathbf{x}) = \nabla_{\mathbf{x}} \cdot \boldsymbol{\sigma}^{\mathrm{p}}(\mathbf{x}) + \mathbf{f}_{\mathrm{m}}(\mathbf{x}), \qquad \nabla_{\mathbf{x}} \cdot \mathbf{u}(\mathbf{x}) = 0. \tag{13}$$

In the above, q is the pressure, μ is the dynamic viscosity, $\boldsymbol{\sigma}^{\mathrm{p}}$ is the extra stress, and $\mathbf{f}_{\mathrm{m}}$ is the force density due to the motors acting at $\mathbf{x}$ on the immersed microtubules. We take the fluid domain to be doubly periodic in x, y with no-slip conditions at the plate $z = -H/2$ and at the cover slip $z = H/2$.

We define the extra stress as $\boldsymbol{\sigma}^{\mathrm{p}} = \boldsymbol{\sigma}^{\mathrm{f}} + \boldsymbol{\sigma}^{\mathrm{t}}$ similar to [8], where $\boldsymbol{\sigma}^{\mathrm{f}}$ arises from microtubule inextensibility and $\boldsymbol{\sigma}^{\mathrm{t}}$ arises from steric interaction. These extra stresses are

$$\boldsymbol{\sigma}^{\mathrm{f}} = \sigma_f \mathbf{S} : \mathbf{E}, \qquad \boldsymbol{\sigma}^{\mathrm{t}} = -\sigma_t [\mathbf{D} \cdot \mathbf{D} - \mathbf{S} : \mathbf{D}], \tag{14}$$

where $\mathbf{E}(\mathbf{x},t) = \frac{1}{2}\left(\nabla \mathbf{u} + \nabla \mathbf{u}^T\right)$ is the rate-of-strain tensor and $\mathbf{S}$ is the fourth order moment of Ψ, $\mathbf{S}(\mathbf{x},t) = \int \Psi \mathbf{pppp} d\mathbf{p}$. The coefficients are $\sigma_f = \pi\mu 4 l^3/3\ln(2r)$ and $\sigma_t = \pi\mu 8 l^3 U_r^0/3\ln(2r)$, which can be derived using slender body theory, with r the microtubule aspect ratio and l the microtubule half-length [8, 27]. While the derivation in [8, 27] is for rods in free space, and our model has walls in the z-dimension, our two-dimensional reduction below (section 2.2) restricts these stress terms to the x, y-plane, for which we use periodic boundary conditions. Therefore we do not derive these coefficients for the case of a nearby boundary. We remark that steric interaction in space does not lead to extra stress terms in the slender body framework, as the resulting force is constant along the microtubule.

In this model, we apply the force spreading approach of the immersed boundary method (see [24]) to our polymeric fluid to obtain the motor force [4]

$$\mathbf{f}_{\mathrm{m}}(\mathbf{x},t) = \iiiint \mathbf{F}(\mathbf{y}, s, \mathbf{p}, \mathbf{r}_0) \delta(\mathbf{y} + s\mathbf{p} - \mathbf{x}) \Psi(\mathbf{y}, \mathbf{p}, t) \mathcal{M}_b(\mathbf{r}_0, s|(\mathbf{y},\mathbf{p}), t) ds\, d\mathbf{r}_0\, d\mathbf{y}\, d\mathbf{p}, \tag{15}$$

where $\mathbf{F}$ is the force associated with a single motor. Further, we note that the convolution with the Dirac-δ function converts from the center-of-mass–based description of Ψ to the spatial description of the force density. The force generated by all bound motor heads acting at $\mathbf{y} + s\mathbf{p}$ is spread to $\mathbf{x}$ by integrating over all possible motor configurations with head at $\mathbf{y} + s\mathbf{p}$. In general, motor stepping speed is load-dependent [14]. However, here we assume that the motor is stepping at a constant speed V_{m}, where its max stepping speed is $V_{\max}$, and thus exerts a constant force of magnitude

$F_{\text{st}}(1-\frac{V_{\text{m}}}{V_{\max}})$ in $-\mathbf{p}$, with F_{st} the motor stall force. This gives the simplified expression for the motor force

$$\mathbf{F}(\mathbf{y}, s, \mathbf{p}, \mathbf{r}_0) = \mathbf{F}(\mathbf{p}) = -F_{\text{st}} \left(1 - \frac{V_{\text{m}}}{V_{\max}}\right) \mathbf{p}. \tag{16}$$

2.2. Two-dimensional reduction. In [12] we showed that to leading order the microtubule orientations are restricted to the x, y-plane. Moreover, experiments have shown that the microtubules and bound motor heads are concentrated about a two-dimensional plane of motion [25]. Taking advantage of this fact obviates the need to track Ψ and $\mathcal{M}_b$ in the z-dimension, which provides critical memory and computation savings when storing and solving for the two distributions. We also restrict the forcing term in the fluid equations to be localized to that plane.

2.2.1. Microtubule distribution. The microtubules are centered around a plane $z = z_0$, where z_0 is about the length of the motor protein, above the bottom plate

$$\Psi(\mathbf{x}, \mathbf{p}, t) = \Psi_{z_0}(\mathbf{x}_2, \mathbf{p}, t)\delta_a(z - z_0). \tag{17}$$

Here δ_a is a smooth delta function, chosen to be

$$\delta_a(z - z_0) = \begin{cases} \frac{1}{2a}(1 + \cos(\frac{\pi(z-z_0)}{a})), & |z - z_0| \le a, \\ 0, & |z - z_0| > a. \end{cases} \tag{18}$$

We note that, to prevent the presence of microtubules or motors at the top or bottom plates of the assay, we further require that $z_0 - a > \frac{-H}{2}$ and $z_0 + a < \frac{H}{2}$. We also introduce the notation $A_i = \int \delta_a^i(z - z_0)dz$ to denote the moments of δ_a. By construction, we have $A_1 = 1$, $A_2 = 3/(4a)$, and $A_3 = 5/(6a)$. Next, the microtubules are constrained to the plane given the geometry of the assay, so $\mathbf{p} = (\cos\theta, \sin\theta, 0)^T$. Defining $\mathbf{p_2} = (\cos\theta, \sin\theta)^T$, we have the decomposition $\Psi_{z_0}(\mathbf{x}_2, \mathbf{p}, t) = \Psi_{z_0}(\mathbf{x}_2, \mathbf{p}_2, t)$.

Using (17), the microtubule reduction proceeds by integrating (1) with respect to z. We use a bar to denote the integral over z of a quantity weighted by the smooth delta function, for example $\bar{\mathbf{u}}(\mathbf{x}_2) = \int \mathbf{u}(\mathbf{x}_2, z)\delta_a(z)dz$. Plugging (17) into (1) and (5)–(7), integrating over z, and using the facts that $\nabla_p = \mathbf{p}_2^{\perp}\partial_\theta$ and that both w and δ_a vanish at the top and bottom plates, we obtain

$$\partial_t \Psi_{z_0} + \nabla_2 \cdot (\dot{\bar{\mathbf{x}}}_2 \Psi_{z_0}) + \partial_\theta(\dot{\bar{\theta}}\Psi_{z_0}) = 0, \tag{19}$$

where we have defined the quantities $\dot{\bar{\mathbf{x}}_2}$ and $\dot{\bar{\theta}}$ as

$$\dot{\bar{\mathbf{x}}}_2 = -V_{\text{sp}}\mathbf{p}_2 + \bar{\mathbf{u}}_2 + A_2 U^0_{t,\|}\mathbf{p}_2\mathbf{p}_2 : \nabla_2 \mathbf{D}_{2,z_0} - D_{\text{t},\|}\nabla_2 \ln \Psi_{z_0}, \tag{20}$$

$$\dot{\bar{\theta}} = (\nabla_2 \bar{\mathbf{u}}_2 + 2U_r^0 A_2 \mathbf{D}_{2,z_0}) : \mathbf{p}_2^{\perp}\mathbf{p}_2 - D_{\text{r}}\partial_\theta \ln \Psi_{z_0}. \tag{21}$$

2.2.2. Bound motor distribution. We make the same assumptions for the bound motor distribution, since the bound motor heads must be in plane with the microtubules they are bound to, and write $\mathcal{M}_b$ analogously to (17) as

$$\mathcal{M}_b(\mathbf{r}_0, s|(\mathbf{x}, \mathbf{p}), t) = \mathcal{M}_{b,z_0}(s, \mathbf{r}_0|\mathbf{x}_2, \theta, t)\delta_a(z - z_0). \tag{22}$$

To derive a reduced equation for the evolved bound motor distribution, we plug the assumptions (22) and (17) into (11), integrate with respect to z, and divide by Ψ_{z_0}. Noting that the set $B_{r_c}(\mathbf{r}_0)$ can be approximated as

$$B_{r_c}(\mathbf{r}_0) \approx \left\{(\mathbf{x}, s, \mathbf{p}) : (\mathbf{x}_2, s, \mathbf{p}_2) \in D_{r_c}(\mathbf{r}_0) \text{ and } -\frac{H}{2} \le z \le -\frac{H}{2} + d_{r_c}(\mathbf{x}_2, s, \theta)\right\},$$

where $D_{r_c}(\mathbf{r}_0) = \{(\mathbf{x}_2, s, \theta) : |\mathbf{x}_2 + s\mathbf{p}_2 - \mathbf{r_0}| < r_c\}$ is the disk of capture radius r_c and $d_{r_c}(\mathbf{x}_2, s, \theta) = \sqrt{r_c^2 - |\mathbf{x}_2 + s\mathbf{p}_2 - \mathbf{r}_0|^2}$, we find

$$\begin{aligned}\partial_t(\mathcal{M}_{b,z_0}) + \partial_s(V_{\mathrm{m}}\mathcal{M}_{b,z_0}) + \dot{\tilde{\mathbf{x}}}_2 \cdot \nabla_2 \mathcal{M}_{b,z_0} - \dot{\tilde{\zeta}}\mathcal{M}_{b,z_0} + \dot{\tilde{\theta}}\partial_\theta \mathcal{M}_{b,z_0} \\ = -k_{\mathrm{off}}\mathcal{M}_{b,z_0} + \frac{k_{\mathrm{on}}}{A_2}\mathcal{M}_f B_2 \mathbb{1}_{D_{r_c}}.\end{aligned} \tag{23}$$

In (23), we defined the tilde quantities similarly to the bar quantities in (20)–(21), but with respect to δ_a^2 as opposed to δ_a. We have

$$\dot{\tilde{x}}_2 = -V_{\mathrm{sp}}\mathbf{p}_2 + \frac{1}{A_2}\tilde{\mathbf{u}}_2 + \frac{A_3}{A_2}U^0_{t,\parallel}\mathbf{p}_2\mathbf{p}_2 : \nabla_2 \mathbf{D}_{2,z_0} - D_{t,\parallel}\nabla_2 \ln \Psi_{z_0}, \tag{24}$$

$$\dot{\tilde{\zeta}} = \frac{1}{2A_2}\widetilde{\partial_z w} - \frac{B_1}{A_2}U^0_{t,\perp}\mathbf{p}_2\mathbf{p}_2 : \mathbf{D}_{2,z_0}, \tag{25}$$

$$\dot{\tilde{\theta}} = \left(\frac{1}{A_2}\nabla_2 \tilde{\mathbf{u}}_2 + 2U_r^0\frac{A_3}{A_2}\mathbf{D}_{2,z_0}\right) : \mathbf{p}_2^\perp \mathbf{p}_2 - D_r \partial_\theta \ln \Psi_{z_0}. \tag{26}$$

The constants B_1 and B_2 are

$$B_1 = \frac{1}{2}\int \delta_a^2(z - z_0)\partial_{zz}\delta_a(z - z_0)dz = -\frac{\pi^2}{4a^4}, \qquad B_2 = \int_{-H/2}^{-\frac{H}{2}+d_{r_c}(\mathbf{x}_2,s,\theta)} \delta_a(z - z_0)dz.$$

While the quantity B_2 is a function of $\mathbf{x}_2$, s, and θ, plugging (18) for δ_a into B_2, integrating, and using a Taylor series expansion of sine yield $0 \le B_2 \le r_c/a$. Therefore, for the remainder of this paper, we let $B_2 = r_c/a$.

Following the same steps for the simplified motor model, we have

$$\mathcal{M}_{b,z_0}(\mathbf{r}_0, s|(\mathbf{x}_2, \theta), t) = \begin{cases} 0 & \text{if } (\mathbf{x}_2, s, \theta) \notin D_{r_c}, \\ H \min\left(C, \frac{\mathcal{M}(\mathbf{r}_0)}{\iiint_{D_{r_c}} \Psi_{z_0} d\mathbf{x}_2 d\theta ds}\right) & \text{if } (\mathbf{x}_2, s, \theta) \in D_{r_c}. \end{cases} \tag{27}$$

2.2.3. Fluid. While we do not average the fluid equations over z, some of the stress and force components are zero as a result of the two-dimensional reduction of $\mathcal{M}_b$ and Ψ. As the stresses are defined in terms of moments of Ψ with respect to $\mathbf{p}$, the implications of (17) for the stress tensors in (14) are

$$\boldsymbol{\sigma}^{\mathrm{f}} = \sigma_f \mathbf{S}_{z_0}(\mathbf{x}_2, t) : \mathbf{E}(\mathbf{x}, t)\delta_a(z - z_0), \tag{28}$$

$$\boldsymbol{\sigma}^{\mathrm{t}} = -\sigma_t \left(\mathbf{D}_{z_0}(\mathbf{x}_2, t) \cdot \mathbf{D}_{z_0}(\mathbf{x}_2, t) - \mathbf{S}_{z_0}(\mathbf{x}_2, t) : \mathbf{D}_{z_0}(\mathbf{x}_2, t)\right) \delta_a^2(z - z_0), \tag{29}$$

where we have defined

$$\mathbf{D}_{z_0}(\mathbf{x}_2, t) = \int \Psi_{z_0}(\mathbf{x}_2, \theta, t)\mathbf{pp}d\theta \quad \text{and} \quad \mathbf{S}_{z_0}(\mathbf{x}_2, t) = \int \Psi_{z_0}(\mathbf{x}_2, \theta, t)\mathbf{pppp}d\theta.$$

We note that the third row and column of $\boldsymbol{\sigma}^{\mathrm{f}}, \boldsymbol{\sigma}^{\mathrm{t}}$ are identically zero because the z-component of $\mathbf{p}$ is zero. Therefore, we use the subscript 2 to denote the upper 2×2 block of each tensor, such as $\mathbf{D}_{2,z_0}$. Since the motor force $\mathbf{F}(\mathbf{p})$ in (16) is in the direction $-\mathbf{p}$, the z-component of $\mathbf{f}_{\mathrm{m}}$ is zero. As a result, the fluid equations (13) take the form

$$-\mu\nabla_2^2 \mathbf{u_2}(\mathbf{x}) - \mu\partial_{zz}\mathbf{u_2}(\mathbf{x}) + \nabla_2 q(\mathbf{x}) = \nabla_2 \cdot \boldsymbol{\sigma}_2^{\mathrm{p}}(\mathbf{x}) + \mathbf{f}_2(\mathbf{x}), \tag{30}$$

$$-\mu\nabla_2^2 w(\mathbf{x}) - \mu\partial_{zz} w(\mathbf{x}) + \partial_z q(\mathbf{x}) = 0, \tag{31}$$

$$\nabla_2 \cdot \mathbf{u_2}(\mathbf{x}) + \partial_z w(\mathbf{x}) = 0, \tag{32}$$

with

$$\mathbf{f}_2(\mathbf{x}) = -F_{\rm st}\left(1 - \frac{V_{\rm m}}{V_{\max}}\right)\delta_a(z-z_0)^2 \iiiint \mathbf{p}_2\delta(\mathbf{y}_2 + s\mathbf{p}_2 - \mathbf{x}_2)\Psi_{z_0}M_{b,z_0}\,ds\,d\mathbf{r}_0\,d\mathbf{y}_2\,d\theta.$$

2.3. Nondimensionalization. In this section, we nondimensionalize the set of reduced equations introduced in section 2.2. To do so, we first introduce the characteristic scales. Let the characteristic length be L in the x, y-dimensions and $H = \varepsilon L$ in the z-dimension ($\varepsilon \ll 1$); let the characteristic velocity be U in the x, y-dimensions and W in the z-dimension; and let the characteristic fluid timescale be $T = L/U$. We set

$$\mathbf{x}_2 = L\mathbf{x}', \quad z = \varepsilon L z' = Hz', \quad \mathbf{u}_2 = U\mathbf{u}_2', \quad w = Ww', \quad t = Tt',$$

where $'$ denotes dimensionless quantities. By a similarity argument, we have that $W = \varepsilon U$.

Since the motors evolve on a smaller scale than the fluid, we introduce new characteristic scales. We take the microtubule half-length l as the length scale, the motor speed $V_{\rm m}$ as the velocity scale for motor evolution, and obtain a new timescale, $\tau = l/V_{\rm m}$. We set

$$s = ls', \quad V = V_{\rm m}V', \quad t = \tau t^*.$$

2.3.1. Microtubule distribution. To nondimensionalize Ψ we recall that it integrates to N, the number of microtubules. Furthermore, since the smooth delta function satisfies $\int \delta_a(z-z_0)dz = 1$, we define Ψ'_{z_0} as

$$\Psi_{z_0}(\mathbf{x}_2, \theta, t) = \frac{N}{L^2}\Psi'_{z_0}(\mathbf{x}_2', \theta, t') \tag{33}$$

so that $\iint \Psi'_{z_0}\,d\mathbf{x}_2'\,d\theta = 1$. Alternatively, if we introduce the nondimensional smooth delta function $\delta'_{a'}(z'-z_0')$ as $\delta_a(z-z_0) = \frac{1}{H}\delta'_{a'}(z'-z_0')$ with $a' = a/H$ to mimic the behavior of a Dirac delta function, then we have for the full nondimensional density of microtubules $\Psi'(\mathbf{x}', \mathbf{p}, t') = \Psi'_{z_0}(\mathbf{x}_2', \theta, t')\delta'_{a'}(z'-z_0')$ and $\iiint \Psi' d\mathbf{x}' d\mathbf{p} = 1$. The microtubule evolution equation (19) is nondimensionalized on the same scale as the fluid equations. Therefore, plugging the definition of the rescaled quantities into (19), (20), and (21) yields

$$\partial_{t'}\Psi'_{z_0} + \nabla_2' \cdot (\dot{\mathbf{x}}_2'\Psi'_{z_0}) + \partial_\theta(\dot{\bar{\theta}}'\Psi'_{z_0}) = 0, \tag{34}$$

$$\dot{\bar{\mathbf{x}}}_2' = -V'_{\rm sp}\mathbf{p}_2 + \bar{\mathbf{u}}_2' + A_2'U_{t,\|}^{0'}\mathbf{p}_2\mathbf{p}_2 : \nabla_2'\mathbf{D}'_{2,z_0} - D'_{\rm t,||}\nabla_2'\ln\Psi'_{z_0}, \tag{35}$$

$$\dot{\bar{\theta}}' = (\nabla_2'\bar{\mathbf{u}}_2' + A_2'U_r^{0'}\mathbf{D}'_{2,z_0}) : \mathbf{p}_2^{\perp}\,\mathbf{p}_2 - D'_{\rm r}\partial_\theta\ln\Psi'_{z_0}, \tag{36}$$

with constants $D'_{\rm t,||} = \frac{D_{\rm t,||}T}{L^2}$, $D'_{\rm r} = D_{\rm r}T$, $U_r^{0'} = \frac{2U_r^0 NT}{HL^2}$, $U_t^{0'} = \frac{U_{t,\|}^0 NT}{HL^4}$, $V'_{\rm sp} = \frac{V_{\rm sp}}{U}$, and $A_2' = \int \delta_{a'}^{'2}(z'-z_0')dz' = HA_2$. We let $\tilde{U_{t,\|}^0} = A_2'U_{t,\|}^{0'}$ to simplify notation. The nondimensional forms of the moment tensors are

$$\mathbf{S}'_{z_0} = \frac{N}{L^2}\mathbf{S}_{z_0}, \qquad \mathbf{D}_{z_0} = \frac{N}{L^2}\mathbf{D}'_{z_0}.$$

2.3.2. Motor distributions. We nondimensionalize the bound motor distribution $\mathcal{M}_b$ so that it integrates to the ratio of bound to total motors:

$$\iiiint \mathcal{M}_b'\Psi' ds'\,d\mathbf{r}_0'\,d\mathbf{x}'\,d\mathbf{p} = \frac{N_b}{N_m} \quad \text{and} \quad \iiiint \mathcal{M}'_{b,z_0}\Psi_{z_0'}ds'd\mathbf{r}_0'd\mathbf{x}_2'd\theta = \frac{N_b}{N_m}.$$

Recalling that $\iiiint \mathcal{M}_b \Psi ds\, d\mathbf{r}_0\, d\mathbf{x}\, d\mathbf{p} = N_b$, plugging in the two-dimensional reductions (17) and (22), and comparing to the above, we obtain

$$\mathcal{M}_{b,z_0}(s, \mathbf{r}_0|(\mathbf{x}_2, \theta), t) = \frac{N_m H}{lL^2 N A_2'} \mathcal{M}'_{b,z_0}(s', \mathbf{r}'_0|(\mathbf{x}'_2, \theta), t^*), \tag{37}$$

and similarly for the full nondimensional distribution,

$$\mathcal{M}'_b(s, \mathbf{r}_0|(\mathbf{x}, \mathbf{p}), t^*) = \frac{1}{A_2'} \mathcal{M}'_{b,z_0}(s, \mathbf{r}_0|(\mathbf{x}_2, \theta), t^*) \delta'_{a'}(z' - z'_0).$$

We rescale the distribution of free motors to the fraction of free motors, setting $\mathcal{M}_f = \frac{N_m}{L^2} \mathcal{M}_f$ and $\mathcal{M} = \frac{N_m}{L^2} \mathcal{M}'$ to obtain

$$\mathcal{M}'_f(\mathbf{r}'_0, t^*) = \mathcal{M}'(\mathbf{r}'_0) - \iiint \mathcal{M}'_{b,z_0} \Psi'_{z_0}\, ds'\, d\mathbf{x}'_2\, d\theta. \tag{38}$$

Using these definitions and the second set of nondimensional variables, we have

$$\begin{aligned} &\partial_{t*} \mathcal{M}'_{b,z_0} + \partial_{s'} \mathcal{M}'_{b,z_0} + \frac{\tau}{T} \dot{\tilde{\mathbf{x}}}'_2 \cdot \nabla_{2'} \mathcal{M}'_{b,z_0} - \frac{\tau}{T} \dot{\tilde{\zeta}} \mathcal{M}'_{b,z_0} + \frac{\tau}{T} \dot{\tilde{\theta}} \partial_\theta \mathcal{M}'_{b,z_0} \\ &\qquad = -k'_{\text{off}} \mathcal{M}'_{b,z_0} + k'_{\text{on}} \mathcal{M}'_f \mathbb{1}_{D_{r'_c}}, \end{aligned} \tag{39}$$

together with the dimensionless fluxes

$$\begin{aligned} \dot{\tilde{\mathbf{x}}}'_2 &= -V'_{\text{sp}} \mathbf{p}_2 + \frac{1}{A_2'} \widetilde{\mathbf{u}}'_2 + \frac{A_3'}{A_2'} U^{0'}_{t,\parallel} \mathbf{p}_2 \mathbf{p}_2 : \nabla_2 \mathbf{D}'_{2,z_0} - D'_{t,\parallel} \nabla'_2 \ln \Psi'_{z_0}, \\ \dot{\tilde{\zeta}}' &= \frac{1}{2A_2'} \widetilde{\partial_{z'} w'} - \frac{B_1' U^{0'}_{t,\perp}}{A_2'} \mathbf{p}_2 \mathbf{p}_2 : \mathbf{D}'_{2,z_0}, \\ \dot{\tilde{\theta}} &= \left(\frac{1}{A_2'} \nabla'_2 \widetilde{\mathbf{u}}'_2 + \frac{A_3'}{A_2'} U^{0'}_r \mathbf{D}'_{2,z_0} \right) : \mathbf{p}_2^\perp \mathbf{p}_2 - D'_r \partial_\theta \ln \Psi'_{z_0} \end{aligned}$$

and constants $A_3' = H^2 A_3$, $U^0_{t,\perp} = \frac{U^0_{t,\perp} NT}{H^3 L^2}$, $B_1' = H^4 B_1$, $k'_{\text{off}} = k_{\text{off}} \tau$, $k'_{\text{on}} = k_{\text{on}} \tau l N r_c / a$. We note that the dot in the above equations refers to a time derivative with respect to t^*. For completeness, we write the definition of the dimensionless disk of radius r'_c centered at $\mathbf{r}'_0$ as

$$D_{r'_c}(\mathbf{r}'_0) = \left\{ (\mathbf{x}'_2, s', \theta) : \left| \mathbf{x}'_2 + \frac{l}{L} s' \mathbf{p}_2 - \mathbf{r}'_0 \right|^2 \le \frac{l^2}{L^2} r'^2_c \right\}.$$

As the bound motor density timescale is approximately a thousand times smaller than the microtubule timescale, we drop most of the terms with $\frac{\tau}{T}$ in (39), except the terms involving the steric parameters $U^{0'}_{t,\parallel}$ and $U^{0'}_r$, as their product with τ/T could end up being order one. We drop the term with $U^{0'}_{t,\perp}$, since our assumption that the motion of the microtubule is constrained to a plane makes it a small number. Eliminating these terms, we have

$$\begin{aligned} &\partial_{t*} \mathcal{M}'_{b,z_0} + \partial_{s'} \mathcal{M}'_{b,z_0} + \frac{A_3'}{A_2'} \frac{\tau}{T} U^{0'}_{t,\parallel} \mathbf{p}_2 \mathbf{p}_2 : \nabla'_2 \mathbf{D}'_{2,z_0} \cdot \nabla_{2'} \mathcal{M}'_{b,z_0} \\ &\qquad + \frac{A_3'}{A_2'} \frac{\tau}{T} U^{0'}_r \mathbf{D}'_{2,z_0} : \mathbf{p}_2^\perp \mathbf{p}_2 \partial_\theta \mathcal{M}'_{b,z_0} = -k'_{\text{off}} \mathcal{M}'_{b,z_0} + k'_{\text{on}} \mathcal{M}'_f \mathbb{1}_{D_{r'_c}}. \end{aligned} \tag{40}$$

Again, for simplicity, we introduce $\widetilde{U^0_{t,\|}} = A'_3\tau U^{0'}_{t,\|}/(A'_2T)$ and $\widetilde{U^0_r} = A'_3\tau U^{0'}_r/(A'_2T)$.

For the simplified motor model, it is straightforward to see that the nondimensional version of (27) is

$$\mathcal{M}'_{b,z_0}(\mathbf{r}'_0, s'|(\mathbf{x}'_2,\theta), t^*) = \begin{cases} 0 & \text{if } (\mathbf{x}'_2, s', \theta) \notin D'_{r'_c}, \\ \min\left(C', \frac{\mathcal{M}'(\mathbf{r}'_0)}{\iiint_{D'_{r'_c}} \Psi'_{z'_0} d\mathbf{x}'_2 d\theta ds'}\right) & \text{if } (\mathbf{x}'_2, s', \theta) \in D'_{r'_c}, \end{cases} \tag{41}$$

where C' is an independent problem-specific parameter.

2.3.3. Fluid. To nondimensionalize the bulk fluid equations, we first rescale the extra stresses as

$$\boldsymbol{\sigma}^{\mathrm{f}} = \sigma'_f \mathbf{S}'_{z_0}(\mathbf{x}_2, t) : \mathbf{E}'(\mathbf{x}, t)\delta'_a(z - z_0), \tag{42}$$

$$\boldsymbol{\sigma}^{\mathrm{t}} = -\sigma'_t \left(\mathbf{D}'_{z_0}(\mathbf{x}_2, t) \cdot \mathbf{D}'_{z_0}(\mathbf{x}_2, t) - \mathbf{S}'_{z_0}(\mathbf{x}_2, t) : \mathbf{D}'_{z_0}(\mathbf{x}_2, t)\right) \delta'^2_a(z - z_0), \tag{43}$$

and $\mathbf{E}(\mathbf{x}, t) = \frac{1}{T}\mathbf{E}'$, where $\mathbf{E}'$ is dimensionless rate-of-strain tensor. Here, we note that the dimensionless gradient of the velocity field has the form

$$\nabla'\mathbf{u}'(\mathbf{x}, t) = \begin{pmatrix} \nabla'_2\mathbf{u_2}' & \frac{1}{\varepsilon}\partial_{z'}\mathbf{u}'_2 \\ \varepsilon(\nabla'_2 w')^T & \partial_{z'}w' \end{pmatrix}.$$

In (42)–(43) the constants are $\sigma'_f = \frac{\sigma_f N}{THL^2}$ and $\sigma'_t = \frac{\sigma t N^2}{H^2L^4}$. Plugging (33) for Ψ and (37) for $\mathcal{M}_b$ into the force density (15), changing variables, and setting $F = F_{\mathrm{st}}\left(1 - \frac{V_{\mathrm{m}}}{V_{\max}}\right)\frac{N_m}{L^2HA'_2}$, we obtain $\mathbf{f}_2(\mathbf{x}, t) = -F\mathbf{f}'_2(\mathbf{x}', t')$, where

$$\mathbf{f}'_2(\mathbf{x}', t') = \delta'^2_{a'}(z' - z'_0) \iiiint \mathbf{p}_2\delta\left(\mathbf{y}'_2 + \frac{l}{L}s'\mathbf{p}_2 - \mathbf{x}'_2\right)\Psi'_{z_0}\mathcal{M}'_{b,z_0} ds' d\mathbf{r}'_0\, d\mathbf{y}'_2\, d\theta.$$

Finally, we plug the nondimensional stresses and forces into the incompressible reduced Stokes equation (30)–(32), and we let the characteristic pressure be P_0 to find ($\varepsilon = H/L$)

$$-\nabla'^2_2\mathbf{u}'_2 - \frac{1}{\varepsilon^2}\partial_{z'z'}\mathbf{u}'_2 + P'_0\nabla'_2 q' = F'\mathbf{f}'_2 + \tilde{\sigma}_f\nabla'_2 \cdot \boldsymbol{\sigma}^{\mathrm{f}'} - \tilde{\sigma}_t\nabla'_2 \cdot \boldsymbol{\sigma}^{\mathrm{t}'}, \tag{44}$$

$$-\nabla'^2_2 w' - \frac{1}{\varepsilon^2}\partial_{z'z'}w' + P'_0\partial_{z'}q' = 0, \tag{45}$$

$$\nabla'_2 \cdot \mathbf{u}'_2 + \partial_{z'}w' = 0. \tag{46}$$

In the above, the constants are $P'_0 = \frac{P_0 L}{\mu U}$, $F' = \frac{FL^2}{\mu U}$, $\tilde{\sigma}_f = \frac{L}{\mu U}\sigma'_f$, and $\tilde{\sigma}_t = \frac{L}{\mu U}\sigma'_t$. In the remainder of this paper and in the supplemental movies at http://www.cs.ucr.edu/~shinar/videos/mtk/mm-gliding-assays.html, we drop all prime, star, tilde, and bar notation and numerically solve the complete set of nondimensional equations, which are summarized in Table 1. For reference, Table 2 lists all parameters and variables used in the model.

3. Implementation. In this section, we discuss the discretization of the nondimensionalized equations summarized in Table 1 and the development of a stable algorithm. Because Ψ_{z_0} and $\mathcal{M}_{b,z_0}$ evolve on two different timescales, we discretize Ψ_{z_0} at time t^n, $n = 0, \ldots, N_T$, with adaptive time step dt and $\mathcal{M}_{b,z_0}$ at time t^m, $m = 0, \ldots, N_{T*}$, with smaller adaptive time step dt^* such that $t^n \le t^m \le t^{n+1}$. After

TABLE 1

Summary of the nondimensionalized model equations for the evolution of microtubules, motors, and fluid in a gliding assay. The primes and nondimensionalizing constants have been dropped for simplicity.

Microtubules

$$\partial_t \Psi_{z_0} + \nabla_2 \cdot (\dot{\mathbf{x}}_2 \Psi_{z_0}) + \partial_\theta (\dot{\theta} \Psi_{z_0}) = 0 \tag{MT1}$$

$$\dot{\mathbf{x}}_2 = -V_{\mathrm{sp}} \mathbf{p}_2 + \mathbf{u}_2 + U^0_{t,\parallel} \mathbf{p}_2 \mathbf{p}_2 : \nabla_2 \mathbf{D}_{2,z_0} - D_{t,\parallel} \nabla_2 \ln \Psi_{z_0} \tag{MT2}$$

$$\dot{\theta} = \nabla_2 \mathbf{u}_2 + U^0_r \mathbf{D}_{2,z_0} : \mathbf{p}_2^\perp \mathbf{p}_2 - D_r \partial_\theta \ln \Psi_{z_0} \tag{MT1}$$

Motors

$$\begin{aligned} &\partial_t \mathcal{M}_{b,z_0} + \partial_s \mathcal{M}_{b,z_0} + U^0_{t,\parallel} \mathbf{p}_2 \mathbf{p}_2 : \nabla_2 \mathbf{D}_{2,z_0} \cdot \nabla_2 \mathcal{M}_{b,z_0} \\ &\quad + U^0_r \mathbf{D}_{2,z_0} : \mathbf{p}_2^\perp \mathbf{p}_2 \partial_\theta \mathcal{M}_{b,z_0} = -k_{\mathrm{off}} \mathcal{M}_{b,z_0} + k_{\mathrm{on}} \mathcal{M}_f \mathbb{1}_{D_{r_c}} \end{aligned} \tag{EM}$$

$$\mathcal{M}_{b,z_0} = \begin{cases} 0 & \text{if } |\mathbf{x}_2 + \frac{l}{L} s \mathbf{p}_2 - \mathbf{r}_0| \geq r_c \\ \min\left(C, \frac{\mathcal{M}(\mathbf{r}_0)}{\iiint_{D_{r_c}} \Psi_{z_0} d\mathbf{x}_2 d\mathbf{p}_2 ds}\right) & \text{if } |\mathbf{x}_2 + \frac{l}{L} s \mathbf{p}_2 - \mathbf{r}_0| < r_c \end{cases} \tag{SM}$$

$$\mathcal{M}_f = \mathcal{M} - \iiint \mathcal{M}_b \Psi_{z_0} \, ds \, d\mathbf{x}_2 \, d\theta \tag{MF}$$

Fluid

$$-\nabla_2^2 \mathbf{u}_2 - \tfrac{1}{\varepsilon^2} \partial_{zz} \mathbf{u}_2 + P_0 \nabla_2 q = \sigma_f \nabla_2 \cdot \boldsymbol{\sigma}^{\mathrm{f}} - \sigma_t \nabla_2 \cdot \boldsymbol{\sigma}^{\mathrm{t}} + F \mathbf{f}_2 \tag{U1}$$

$$-\nabla_2^2 w - \tfrac{1}{\varepsilon^2} \partial_{zz} w + P_0 \partial_z q = 0 \tag{U2}$$

$$\nabla_2 \cdot \mathbf{u}_2 + \partial_z w = 0 \tag{U3}$$

Force

$$\mathbf{f}_2 = F \delta_a^2 (z - z_0) \iiint\!\!\iint \mathbf{p}_2 \delta(\mathbf{y}_2 + \tfrac{l}{L} s \mathbf{p}_2 - \mathbf{x}_2) \Psi_{z_0} \mathcal{M}_{b,z_0} \, ds \, d\mathbf{r}_0 \, d\mathbf{y}_2 \, d\theta \tag{F1}$$

initializing Ψ_{z_0} and $\mathcal{M}_{b,z_0}$, we calculate the initial time step dt and, if the evolved motor model is being used, the initial time step dt^* as well. The motor forces and steric stresses are computed next and used to solve the fluid equations. The new fluid velocities are used to update Ψ_{z_0} to time $t + dt$, and finally M_{b,z_0} is updated to time $t + dt$ based on the updated Ψ_{z_0}. New time steps are computed, and the simulation continues. The procedure is summarized in Algorithm 1, and details are given below. Our numerical scheme is similar to that of our previous scheme in [12]. The primary differences are that the fluid equations are now solved in three dimensions, and that extra stress terms resulting from the steric interactions are included.

To compute the time step dt, we calculate the maximum of the angular and linear advection velocities in (33) and adjust the time step according to the CFL condition. To find the small time step for $\mathcal{M}_b$, we limit the fraction of available motors that can bind or unbind in any given time step. To calculate dt^*, we compare the change due to s-advection with the greatest change due to binding and unbinding, and use the more restrictive of the two to clamp dt^*.

3.1. Microtubule density. We discretize $\Psi_{z_0}(\mathbf{x}_2, \theta)$ over the domain $(\mathbf{x}_2, \theta) \in [-1, 1]^2 \times [0, 2\pi]$ at the plane of motion $z = z_0$ with a triply periodic grid of size $N_x \times N_y \times N_\theta$, with $N_x = N_y$. The advection terms in (MT1) (Table 1) are discretized spatially with an upwinding scheme and Superbee flux limiter [7]. The equation (MT1) is integrated in time using second order Adams–Bashforth method for the advective terms and Crank–Nicolson for the diffusive terms. The resulting system

TABLE 2
Model parameters and variables.

Ψ	Microtubule density
$\mathbf{x}, \mathbf{p}$	Three-dimensional position and orientation
θ	In-plane orientation angle
$\dot{\mathbf{x}}, \dot{p}$	Microtubule linear and angular velocity
V_{sp}	Microtubule self-propulsion velocity
N	Total number of microtubules
$\boldsymbol{\sigma}^{\mathrm{f}}, \boldsymbol{\sigma}^{\mathrm{t}}, \boldsymbol{\sigma}^{\mathrm{p}}$	Microtubule inextensibility stress, steric interaction stress, and combined total stress
σ_f, σ_t	Inextensibility and steric interaction stress coefficients
$\mathbf{u}, q, \mu$	Fluid velocity, pressure, and viscosity
U_t, U_r	Translational and rotational steric potentials
K_t, K_r	Maier–Saupe translational and rotational steric potentials
$D_{\mathrm{t},\perp}, D_{\mathrm{t},\|\|}, D_{\mathrm{r}}$	Linear perpendicular diffusion, linear parallel diffusion, and rotational diffusion
$\mathbf{D}, \mathbf{S}$	Second and fourth moments of Ψ with respect to $\mathbf{p}$
$\mathbf{E}$	Rate-of-strain tensor
$\mathcal{M}, \mathcal{M}_f, \mathcal{M}_b$	Total motor density, free motor density, and bound motor density per microtubule
r_c	Motor protein capture radius
$\mathbf{r}_0$	Motor protein tail position
z_0	Height above bottom of assay at which microtubules and bound motor protein heads are centered
$B_{r_c}(\mathbf{r}_0)$	Allowable configurations $\mathbf{x}, \mathbf{p}, s$ of bound motors in a ball of radius r_c around $\mathbf{r}_0$
$D_{r_c'}(\mathbf{r}_0')$	Dimensionless disk of radius r_c' centered at $\mathbf{r}_0'$
$k_{\mathrm{on}}, k_{\mathrm{off}}$	Motor protein binding and unbinding rates
C	Simplified motor model binding coefficient
δ, δ_a	Dirac delta and smooth Dirac delta function
$\mathbf{f}$	Bound motor force on fluid
$\mathbf{F}$	Force associated with a single motor
F_{st}	Motor protein stall force magnitude
L, H, U, P_0, T	Macroscopic characteristic scales: assay length and height, fluid velocity, pressure, and time
ε	Ratio between assay height and length ($H = \varepsilon L$)
l, V_m, τ	Microscopic characteristic scales: microtubule half-length, motor stepping speed, and motor evolution time

of equations for Ψ_{z_0} is solved using the conjugate gradient method with incomplete Cholesky factorization used as a preconditioner.

3.2. Motor distributions. To advance $\mathcal{M}_{b,z_0}$ forward in time according to the evolved motor model (EM) in Table 1, two-step Adams–Bashforth with variable time step dt^* is used to discretize the s-advection term and the binding and unbinding terms. We clamp $\mathcal{M}_{b,z_0}(\mathbf{r}_0, s|\mathbf{x}_2, \theta)$ so that $\iiint \mathcal{M}_{b,z_0}\Psi_{z_0}\, ds\, d\mathbf{x}_2\, d\theta \leq \mathcal{M}(\mathbf{r}_0)$.

The bound motor density $\mathcal{M}_{b,z_0}$ is high-dimensional as it tracks motor tail position, the filament arclength parameter, and the center of mass and orientation of the filament the bound motor head is attached to. However, since a head detaches if the elongation of the motor stalk exceeds a certain threshold, $\mathcal{M}_{b,z_0}$ can be computed and stored sparsely in a local grid around $\mathbf{r}_0$. The specific condition $\mathbf{x}_2 + \frac{l}{L}s\mathbf{p}_2 - \mathbf{r}_0 \leq r_c$ allows further pruning of this localized configuration space. In our formulation, the activity of the motors anchored at $\mathbf{r}_0$ is independent of motors anchored elsewhere. In discrete form each cell $\mathbf{y}$ stores the local grid over $\mathbf{x}, \theta, s$ for bound motors whose tails are anchored anywhere within the boundaries of cell $\mathbf{y}$. Each cell's motor dis-

Algorithm 1. Numerical evolution scheme for the coupled microtubule density, motor protein distribution, and fluid velocity equations.

```
Initialize Ψ_{z_0} and M_{b,z_0}.
Precompute LU-decomposition of semispectral matrices for all frequency pairs.
while t < t_end do
  Compute adaptive dt.
  Compute Ψ_{z_0}(t+dt) by solving (MT1)–(MT3) using second order Crank–Nicolson
  for the diffusive terms and Adams–Bashforth 2 for the advection terms.
  if (using EM) then
    Set t*_end = t + dt.
    while t* < t*_end do
      Compute adaptive dt*.
      Compute M_{b,z_0}(t* + dt*) by solving (EM) with Adams–Bashforth 2.
      Update M_f from M_{b,z_0} with (MF).
    end while
  else if (using simplified motor model) then
    Solve (SM).
    Update M_f from M_{b,z_0} with (MF).
  end if
  Calculate extra stresses.
  Calculate motor force (F1) using trapezoidal rule and a local grid.
  Solve semispectral (U1)–(U3).
end while
```

tribution is updated in parallel. $\mathcal{M}_{b,z_0}$ is stored as a two-dimensional array over $\mathbf{r}_0$, each containing an unrolled flat array for $\mathbf{x}_2, s, \theta$. We solve the evolved motor density equation on the GPU, where each $\mathbf{r}_0$ is updated in single instruction, multiple data (SIMD) fashion by several threads. Another advantage to this layout is that $\mathcal{M}_{b,z_0}$ independent outermost two-dimensional arrays can be split up and sent to multiple GPUs, or solved in batches on a single GPU if the shared memory is exceeded. As grid resolution increases, the three copies of $\mathcal{M}_{b,z_0}$ at the current and two previous times required by the two-step Adams–Bashforth time integration scheme may not all fit onto the GPU on-board memory simultaneously and instead need to be solved a few rows at a time.

Since we do not track free motor heads, we can discretize the distribution of free motors $\mathcal{M}_f$ and total motors $\mathcal{M}$ over a uniform grid of size $N_x \times N_y$. Updating $\mathcal{M}_f$ from $\mathcal{M}$ and $\mathcal{M}_{b,z_0}$ is straightforward and parallelizable over $\mathbf{x}_2$ by evaluating the discretized form of (MF) in Table 1.

3.3. Fluid. We discretize the domain into $N_x \times N_y \times N_z$ grid cells, where $N_x = N_y$, and solve for the fluid state at each discrete time t^n. $\mathbf{u}_2$ and q are sampled at cell centers, while w is sampled at the z faces. As we have periodic boundary conditions in the $\mathbf{x}_2$-plane, we use a semispectral approach and take the Fourier transform in $\mathbf{x}_2$

of (U1)–(U3), giving for each frequency pair $\mathbf{k} = (k_x\, k_y)^T$

$$\left(|\mathbf{k}|^2 - \frac{1}{\varepsilon^2}\partial_{zz}\right)\hat{\mathbf{u}}_2^n + iP_0\hat{q}^n\mathbf{k} = F\hat{\mathbf{f}}_2^n + i\sigma_f\hat{\boldsymbol{\sigma}^{\mathrm{f}}}^n\mathbf{k} + i\sigma_t\hat{\boldsymbol{\sigma}^{\mathrm{t}}}^n\mathbf{k}, \tag{47}$$

$$\left(|\mathbf{k}|^2 - \frac{1}{\varepsilon^2}\partial_{zz}\right)\hat{w}^n + P_0\partial_z\hat{q}^n = 0, \tag{48}$$

$$i\mathbf{k}\cdot\hat{\mathbf{u}}_2^n + \partial_z\hat{w}^n = 0. \tag{49}$$

Equations (47)–(49) yield an independent $(4N_z - 1) \times (4N_z - 1)$ linear system for each frequency pair. This formulation is computationally advantageous for several reasons. First, the equations for each $\mathbf{k}$ can be solved independently, allowing simple parallelization. Second, the coefficient matrix of each linear system is constant in time, and an LU-factorization for each can be precomputed and stored. We can reasonably store $N_x \times \frac{N_y}{2}$ separate $(4N_z - 1) \times (4N_z - 1)$ matrices and use them to solve for multiple right-hand sides. The FFTW library [9] is used with precomputed transformation mappings to efficiently perform the FFT and inverse FFT.

As the microtubules are concentrated around the $z = z_0$-plane, it is desirable to have more accuracy there and in the thin δ_a-width region around it than in the distant assay regions above and below it. Given the aforementioned scaling of each frequency pair fluid solve matrix with N_z^2, we use a nonuniform grid with variable spacing in the z-dimension. We store $\hat{\mathbf{u}}_2$, and $\hat{q}$ at the z-cell centers, and $\hat{w}$ at the z-cell faces. A schematic of the z-grid is shown in Figure 3.

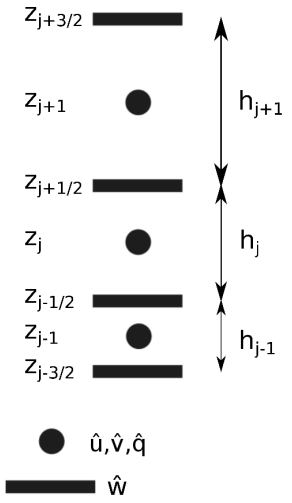

FIG. 3. *Schematic of the nonuniform staggered grid in z used to store the spectral values of* $\hat{\mathbf{u}}, \hat{w}, \hat{p}$.

To compute second derivatives with respect to z at a z-cell j, we construct a fourth order Lagrange interpolating polynomial using z_{j-2}, z_{j-1}, z_j, z_{j+1}, z_{j+2} and differentiate twice. Near the boundaries, we use boundary data and the no-slip boundary condition for the extreme samples and drop to third order interpolation for the bottom-most and top-most equations. For first derivatives at a z-face $j+1/2$, we construct a third order Lagrange interpolating polynomial using z_{j-1}, z_j, z_{j+1}, z_{j+2} and differentiate once. Near the boundaries, we use the nearest four samples to construct the interpolating polynomial. We find that our semispectral fluid solver is second order accurate.

The motor force calculation is the single most computationally intense portion of the algorithm because the force spreading dictates that nearby forces be calculated in order to determine the total force at $\mathbf{x}$. In terms of implementation, this effectively increases the already high dimensionality of the bound motor distribution, whether it is approximated with the simple motor model or the evolved motor model. To account for the motor force's highly parallel but computationally intensive nature, it is calculated on a GPU using a scheme similar to the bound motor solve described above. A speedup of roughly forty times relative to a single-core implementation is observed.

Computation of the stress tensors is straightforward and parallelizable. $\boldsymbol{\sigma}^{\mathrm{f}}$ depends on the rate-of-strain tensor $\mathbf{E}$, which we have only for the previous time step since we compute the extra stresses before the fluid solve. We therefore linearly extrapolate $\mathbf{E}$ at the new time $t + dt$ using the current and previous values, as in [8].

4. Results. In this section, we present results for various experiments with the following parameters held constant: 2μm-length microtubules, $k_{\mathrm{on}} = 25$, $k_{\mathrm{off}} = .1$, $U_t = -.01$, $125{\times}125\mu\mathrm{m}^2$ assay, $N_m = 3{\times}10^6$ motors, $V_{\max} = 1\mu\mathrm{m}s^{-1}$, and $N = 22300$ microtubules. Our nonuniform z-grid has 30 evenly sized fine z-cells covering the range $\{-.5, -.4\}$, with $z_0 = \frac{-h}{2} + .05 = -.45$ in the middle. Above $z = -.4$, the height of each cell doubles consecutively until the cell size is sixteen times greater than that of the fine z-cells at the bottom. Our final 3D grid dimensions are $128 \times 128 \times 49$, with 32 cells in s and θ, at which we find the qualitative features to be well resolved.

In the figures, we plot the nondimensionalized spatial microtubule distribution

$$\Psi_{\mathrm{spatial},z_0}(\mathbf{x}_2, t) = \int \Psi_{z_0}(\mathbf{x}_2, \theta, t) d\theta \tag{50}$$

with color ranging from white (low) to blue (high). We plot the nondimensional spatial bound motor distribution

$$\mathcal{M}_{\mathrm{b,spatial},z_0}(\mathbf{r}_0, t) = \iiint \mathcal{M}_{b,z_0}(s, \mathbf{r}_0, t|\mathbf{x}_2, \theta)\Psi_{z_0}(\mathbf{x}_2, \theta, t) ds d\mathbf{x}_2 d\theta \tag{51}$$

with color ranging from tan (low) to red (high). The colorbars are annotated with the corresponding percentage of the total available motors in the bound configuration, at the low and high ranges of each normalization. Finally, we compute the orientation matrix

$$\mathbf{N}(\mathbf{x}_2, t) = \frac{\int \mathbf{p}_2 \mathbf{p}_2^T \Psi_{z_0}(\mathbf{x}_2, \theta, t) d\theta}{\int \Psi_{z_0}(\mathbf{x}_2, \theta, t) d\theta} \tag{52}$$

and draw its eigenvectors in red scaled by their associated eigenvalues. When present, velocity vectors (black) and orientation eigenvectors are plotted for every fifth cell for clarity.

4.1. Evolved motor model.

Single clump. We first examine the processive behavior of a clump of aligned filaments as the steric alignment parameter is varied between $U_r = 0$ and .01. We present results for $U_r = 0$, .01 and the evolved motor model in Figure 4. We observe that as U_r increases to .01 the clump better maintains its shape, whereas at $U_r = 0$ microtubules become concentrated along the leading edge of the clump, which assumes a widening crescent-like shape. The bottom row of Figure 5 shows the microtubule orientation field at the final frame displayed in the upper rows with $U_r = 0$ (left)

and $U_r = .01$ (right). For higher values of U_r, the microtubule orientation field is uniformly aligned. For smaller values of U_r, the microtubule orientation field at the clump's leading edge becomes tangential to the leading edge, as the rods rotate to avoid compression or extension by the steep velocity gradient, clearly visible in the $U_r = 0$ case. For $U_r = .01$, the steric resistance to rotatation relative to neighboring microtubules counteracts this effect, and the orientation field remains more uniform. In vitro experiments have shown shape persistence in aligned clumps [29], qualitatively similar to the $U_r = .01$ case.

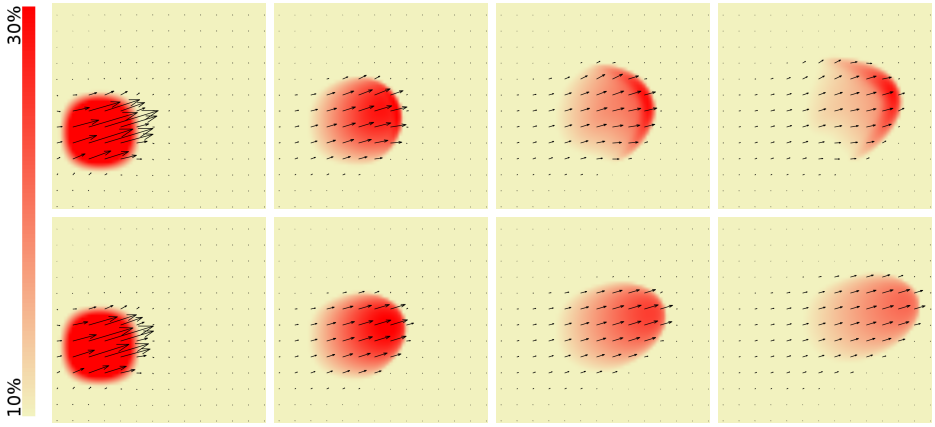

FIG. 4. *Single aligned microtubule clump simulation with evolved motor model. Bound motor protein density visualized with gradient from tan (low) to red (high). Fluid velocity plotted as a black arrow every fifth cell. First row:* $U_r = 0$. *Second row:* $U_r = .01$. *Images are at times* $t = 0$, 15, 30, *and* 45 *s. (See online version for color.)*

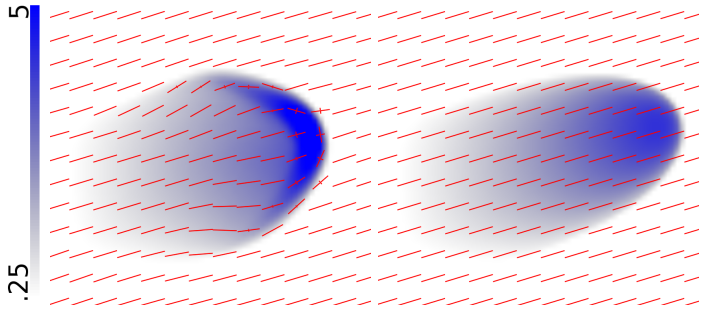

FIG. 5. *Single aligned microtubule clump simulation with evolved motor model. Microtubule density visualized with gradient from white (low) to blue (high). Microtubule orientation eigenvectors plotted as red vectors every fifth cell. Simulation shown at time* $t = 45\,s$ *for* $U_r = 0$ *(left) and* $U_r = .01$ *(right). (See online version for color.)*

Colliding clumps. We examined the behavior of colliding clumps for three values of the steric alignment parameter $U_r = 0, .001, .01$ and both head-on and perpendicular collisions. When clumps collide, the behavior depends on the angle between the microtubule orientations of the clumps.

A nearly perpendicular collision, as in Figure 6, results in the clumps merging and moving as a single clump for all U_r tested. While the U_r term drives local alignment,

alignment also occurs in the $U_r = 0$ case as follows. When the self-propulsion velocity is zero, microtubules move passively with the flow. As motor forces act directly on the fluid, motor forces acting in opposite directions cancel out. This cancellation occurs in the example depicted in Figure 6, where the resultant force points in the average direction of the colliding microtubule orientations—in this case, upwards. These two mechanisms give different qualitative results, as illustrated in Figure 6. In the $U_r = 0$ case (third row), the microtubule distribution remains isotropic as long as local fluid flow remains negligible, whereas in the $U_r = .01$ case (fourth row), we observe steric alignment of the microtubules throughout the entire domain. Higher U_r results in steeper gradients in microtubule orientation and density at the midline. The higher concentration in turn leads to stronger motor forces and higher fluid velocities. These U_r-dependent collision phenomena are observed wherever two regions of dense microtubules collide.

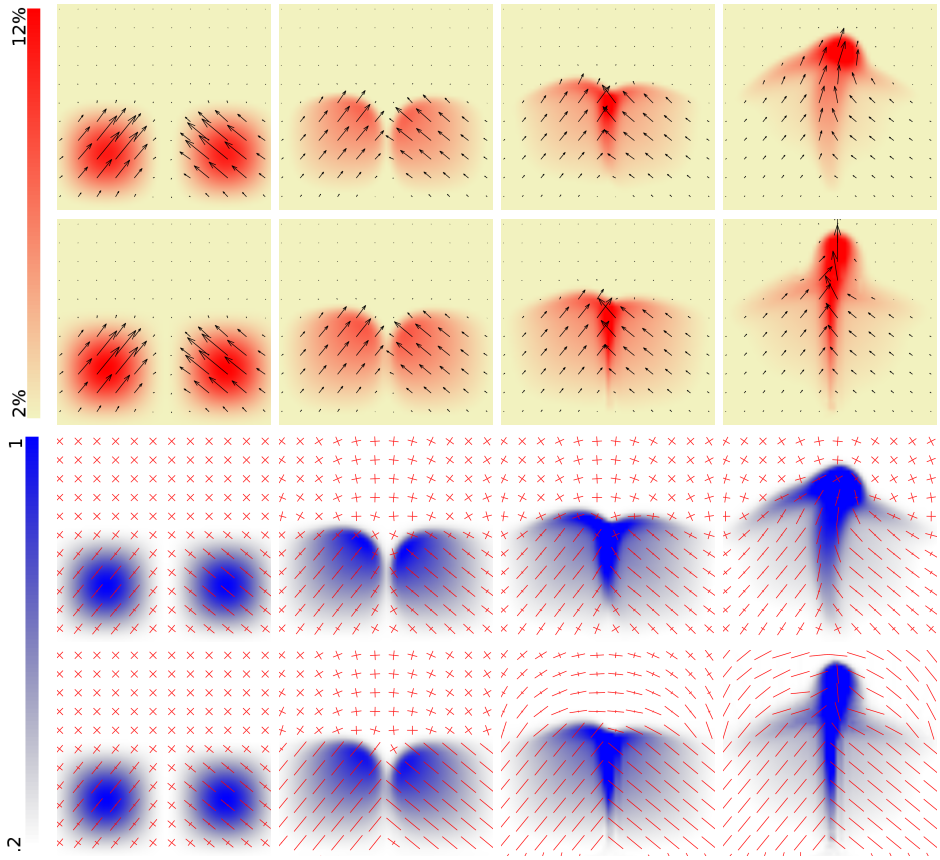

FIG. 6. *Nearly perpendicular microtubule clumps driven by the evolved motor model colliding. First row: $U_r = 0$ velocity field. Second row: $U_r = .01$ velocity field. Third row: $U_r = 0$ orientation field. Fourth row: $U_r = .01$ orientation field. Images are at times $t = 0$, 45, 90, and 180 s.*

In the case of two clumps with antiparallel orientations colliding close to head-on (Figure 7 and supplemental movie 1, first example), significant differences are observed for $U_r = 0$ versus $U_r = .01$. In the $U_r = 0$ case, the motor forces drive an extensional fluid flow on either side of the collision centerline, creating two clumps moving in

opposite directions. In the case $U_r = .01$, the steric force prevents alignment with the extensional flow, and the microtubules of each clump slide past each other. As a result of slight differences in the original clump position, the clumps break down after collision, and smaller clumps pass through each other and continue along the initial clump trajectories. The orientation field (Figure 7, fourth row) shows that the microtubules do not rotate during the initial collision and its aftermath.

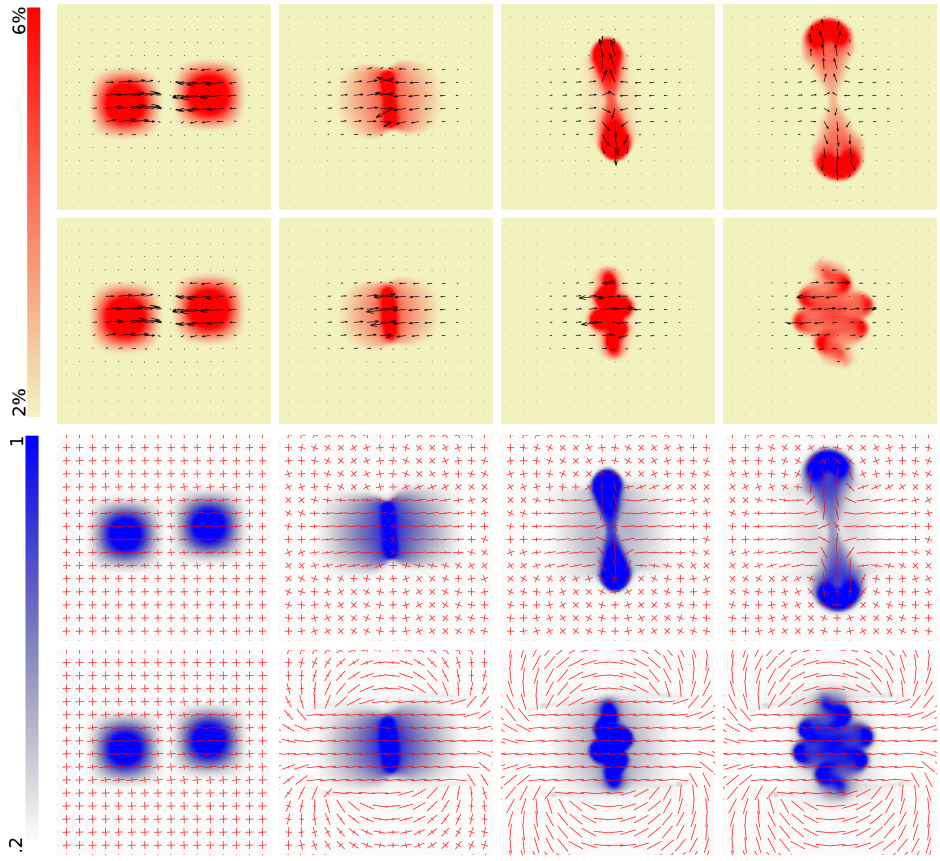

FIG. 7. *Antiparallel microtubule clumps driven by the evolved motor model colliding. First row:* $U_r = 0$ *velocity field. Second row:* $U_r = .01$ *velocity field. Third row:* $U_r = 0$ *orientation field. Fourth row:* $U_r = .01$ *orientation field. Images are at times* $t = 0$, 90, 180, *and* 270 *s. See supplemental movie* 1, *first example.*

Vortex lattice. To test our model's ability to reproduce characteristics of the lattice of vortices observed in [33], we simulate four overlapping rings of microtubules oriented in clockwise fashion, as shown in Figure 8 and the first example in supplemental movie 2. In the overlapping regions, the microtubules from adjacent rings are oriented opposite each other. We observe extensional flow in the dense overlapping regions combined with counterclockwise rotation driven by the initial orientations. With $U_r = 0$ the rotational flow develops four vortices rotating clockwise centered about the spaces between the initial four vortices. The new vortices contract then expand outward until they develop overlapping regions moving in opposite directions, similar to the initial condition. The process repeats itself; extensional flow and rota-

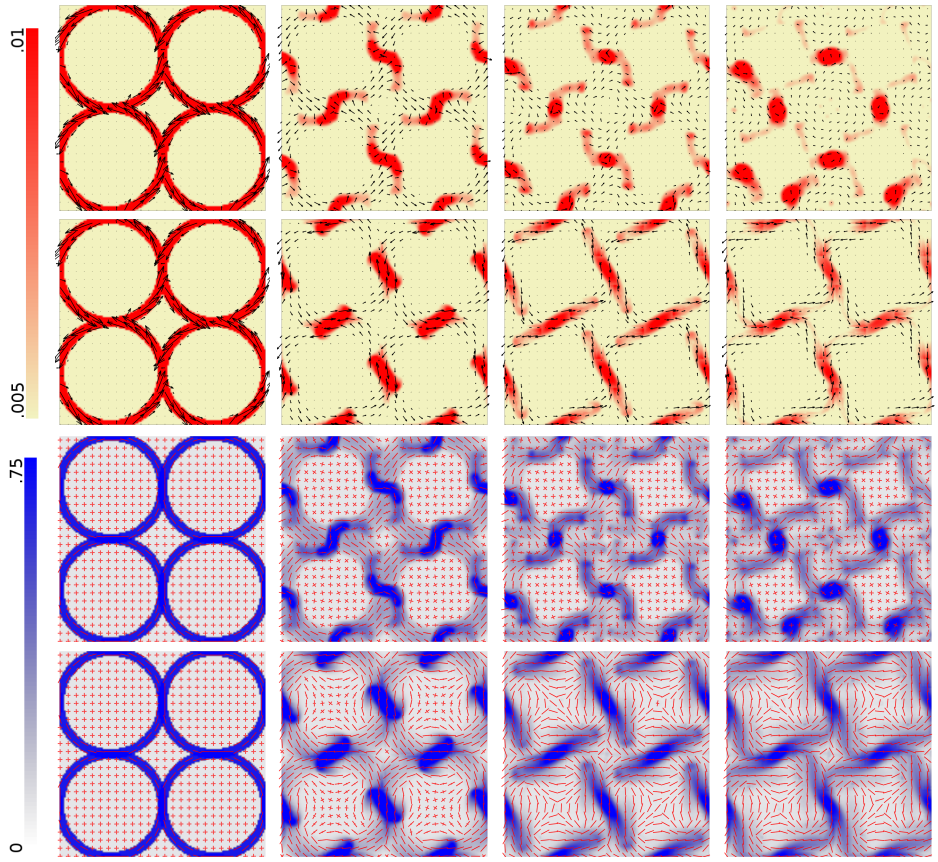

FIG. 8. *Vortex lattice experiment with evolved motor model. First row:* $U_r = 0$ *velocity field. Second row:* $U_r = .01$ *velocity field. Third row:* $U_r = 0$ *orientation field. Fourth row:* $U_r = .01$ *orientation field. Images are at times* $t = 0$, 240, 480, *and* 720 *s. See supplemental movie* 2, *first example.*

tion form again in the overlapping regions, leading to the formation of four vortices rotating counterclockwise at the original four vortex locations. Due to diffusion, the maximum concentration and hence velocity decrease on average throughout the process. Due to symmetry breaking, the transition from vortices with overlapping regions to new vortices with overlapping regions and opposite rotation repeats a few times at most, depending on parameters, until the original structure is lost. Increasing U_r from 0 to .01 increases the maximum microtubule density and flow velocity and gives steeper gradients in microtubule concentration and orientation, as seen in previous examples. It also affects the degree to which the initial dense overlapping regions break down with the rotational forcing from the motor proteins. In particular, for $U_r = .01$ (Figure 8, second and fourth rows), the dense overlapping regions extend but do not separate, and thus preserve much of the original four vortex structure. With the inclusion of the steric interaction term, our results are more consistent with the experiments of [33], which demonstrate a temporally persistent lattice of vortices.

Perturbation. We perturb a uniform isotropic microtubule density in both space

and orientation by adding

$$\frac{1}{a}\sum_{i,j=1}^{8}\epsilon_{ij}\cos(\pi ix+\xi_{ij})\cos(\pi jy+\xi_{ij})P_{ij}(\theta), \tag{53}$$

where ϵ_{ij} is a uniform random number in $[-.001,.001]$, ξ_{ij} is a uniform random number in $[0,2\pi]$, a is a normalization constant, and $P_{ij}(\theta)$ are third order polynomials in $\cos(\theta)$ and $\sin(\theta)$ with random coefficients in $[-1,1]$. The $U_r=0$ case results in a spatiotemporally stable Ψ_{z_0} density (Figure 9, supplemental movie 3). In the $U_r=.01$ case, continuous narrow tracks of stationary microtubules form and remain stable.

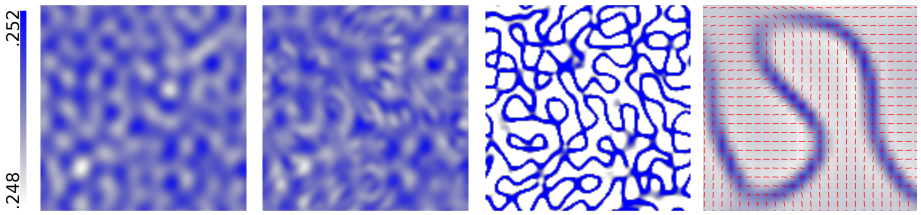

FIG. 9. *Perturbation in x and θ giving rise to stationary concentrated pattern with $U_r=.01$ for the evolved motor model. First three images: evolution of microtubule density in time. Fourth image: magnified section of final top-row image with orientation eigenvectors in red. The microtubule density concentrates along steep gradients in the microtubule orientation field. Images are at times $t=0$, 75, and 113 s. See supplemental movie 3. (See online version for color.)*

4.2. Evolved motor model with self-propulsion.

Colliding clumps. We repeat the antiparallel colliding clumps experiment with the addition of a phenomenological self-propulsion velocity $V_{\rm sp}$ (see (2), (MT2)) in Figure 10 and the second two examples in supplemental movie 1. In the case of $V_{\rm sp}=0$, illustrated in Figure 7, the clumps break up as they collide. At $V_{\rm sp}=1$ and $U_r=.01$, the clumps pass through each other largely intact. For $V_{\rm sp}=1$ and $U_r=0$, we see a combination of both effects, with some passthrough and some spreading of microtubules with the extensional flow formed in the collision. In general, varying the value of $V_{\rm sp}$ between 0 and 1 leads to a corresponding combination of the extreme $V_{\rm sp}=0$ and $V_{\rm sp}=1$ behaviors. The experiments of [29] demonstrate a combination of passthrough and breakup when clumps collide. Experiments of the behaviors of microtubules undergoing collisions [33] show that colliding microtubules can merge and realign or pass through depending on the angle of collision. With the addition of a self-propulsion term, our numerical experiments reproduce such behaviors.

Vortex rings. We repeat the four ring vortex experiment with the addition of a self-propulsion velocity $V_{\rm sp}$ (Figure 11 and second and third examples in supplemental movie 2). With $V_{\rm sp}=.1$ and $U_r=0$, depicted in the first row, motor forces at the overlapping regions of the initial rings create a shear flow that separates these regions and, in conjunction with the self-propulsion, creates counterclockwise vortices at the separatrix between clockwise vortices, as seen in the second image of the first row. This separates the dense bands of microtubules into two connected bands that translate and rotate away from each other, eventually meeting other bands at the centers of the original rings in a cross-like pattern (third image). The microtubules gather at the centers of the crosses, then reverse direction and expand outward in a nonsymmetric way (fourth image), similar to the switching behaviors observed when the experiment is run without self-propulsion (Figure 8). With $V_{\rm sp}=.1$ and $U_r=.01$, depicted in the second row, the steric alignment prevents the shear flow from separating the initial

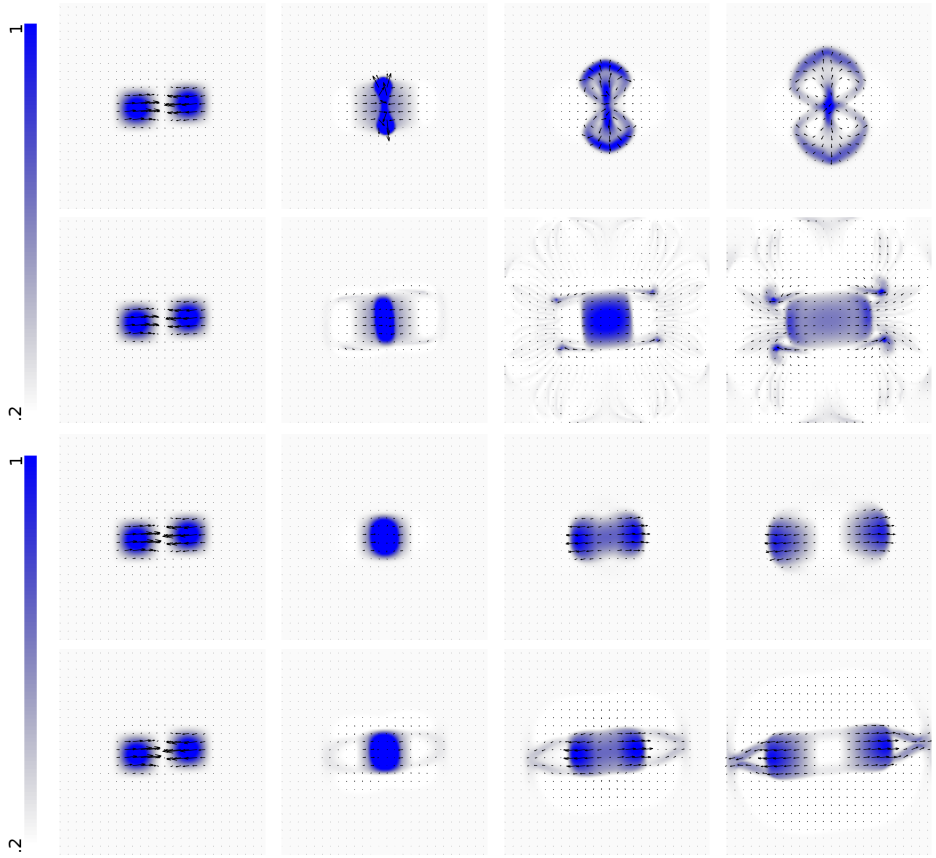

FIG. 10. *Colliding clump experiment with added self-propulsion velocity. First row:* $U_r = 0$ *and* $V_{sp} = .1$. *Second row:* $U_r = .01$ *and* $V_{sp} = .1$. *Third row:* $U_r = 0$ *and* $V_{sp} = 1$. *Fourth row:* $U_r = .01$ *and* $V_{sp} = 1$. *Images are at times* $t = 0, 105, 210, 315\,s$ *in the first and second rows, and at* $t = 0, 24, 48, 72\,s$ *in the third and fourth. See the second and third examples in supplemental movie* 1.

overlapping regions, and the self-propulsion drives antiparallel sliding that stretches the dense microtubule regions into long cohesive bands (second image, second row). The bands break down into smaller clumps (third image), but the steric alignment term keeps the new clumps following the paths of the initial bands, which roughly correspond with the initial four vortex structure (fourth image) as observed without self-propulsion (Figure 8). Increasing the self-propulsion velocity to $V_{\text{sp}} = 1$ causes the self-propulsion to dominate the effects of the motor forces, so microtubule passthrough (with alignment if $U_r > 0$) becomes dominant. With $U_r = 0$ (third row), switching events occur continuously, and the four quadrants of the assay are symmetric. We observe that with $U_r = .01$, passthrough rapidly breaks up the ring structure (fourth row). As a result, no switching events occur.

Perturbation. We repeat the perturbation experiment with the addition of a self-propulsion velocity V_{sp} (Figure 12 and second and third examples in supplemental movie 3). At $V_{\text{sp}} = 1$ or .1 and $U_r = 0$, the clumps translate but simply pass through one another without increasing in density or aligning. With $V_{\text{sp}} = .1$ and $U_r = .01$ (first row), we get fast translational microtubule bands, as opposed to the stationary

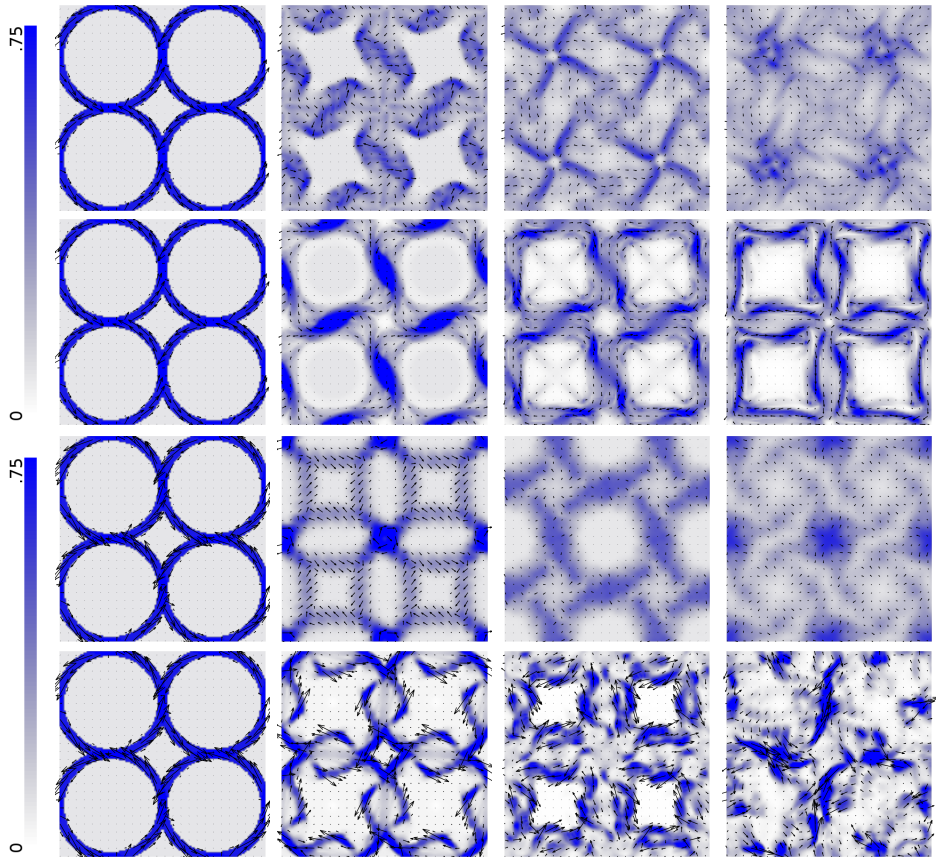

FIG. 11. *Vortex ring experiment with added self-propulsion velocity. Images are illustrative of behavior and thus are not necessarily taken at the same simulation time between rows. First row:* $U_r = 0$ *and* $V_{sp} = .1$. *Second row:* $U_r = .01$ *and* $V_{sp} = .1$. *Third row:* $U_r = 0$ *and* $V_{sp} = 1$. *Fourth row:* $U_r = .01$ *and* $V_{sp} = 1$. *Images are at times* $t = 0, 225, 450, 675\,s$ *in the first two rows, and at* $t = 0, 60, 120, 180\,s$ *in the third and fourth. See second and third examples in supplemental movie* 2.

continuous tracks in the $V_{\text{sp}} = 0$ case shown in Figure 9. At $V_{\text{sp}} = 1$ and $U_r = .01$ (second row), the bands form faster and are denser than in the $V_{\text{sp}} = .1$ case.

4.3. Simplified motor model.

Vortex rings. For the parameters, experiments, and timescales presented here, the differences in density, feature shape, and location observed between the microtubule distribution fields generated by the simplified and evolved motor models are minor. One notable exception is that, in the vortex ring experiment, the evolved motor model drives clockwise rotation in the four central clumps, whereas the simplified motor model drives counterclockwise rotation (Figure 13). This effect is due to a slight difference in the motor force pattern around each clump. On timescales longer than those presented in this work, simulations may eventually show significant divergence.

Colliding clumps. Results from the antiparallel colliding clump simulation driven by the simplified motor model are presented in Figure 14 (and supplemental movie 4) for values of the parameter $C = 10, 50, 250$. Increasing C not only increases the fluid velocities in the simulation by increasing the value of $\mathcal{M}_{b,spatial,z_0}$ for a given Ψ_{z_0},

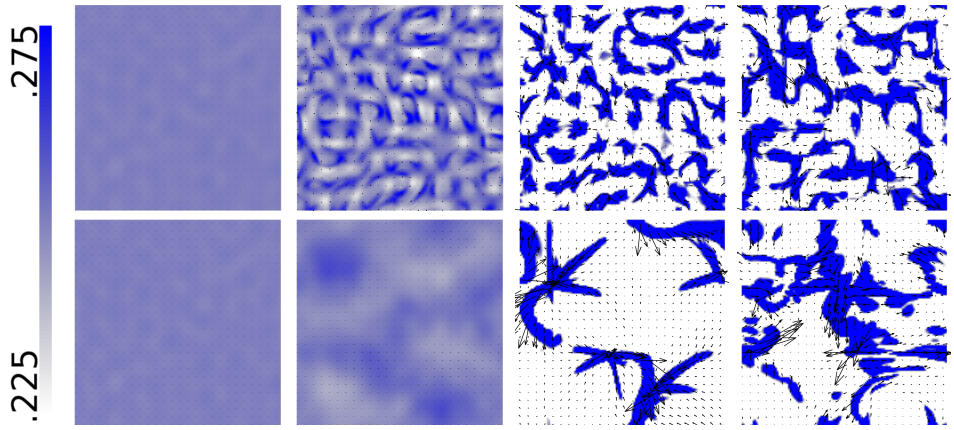

FIG. 12. *Perturbation experiment with added self-propulsion velocity. First row:* $U_r = .01$ *and* $V_{sp} = .1$. *Second row:* $U_r = .01$ *and* $V_{sp} = 1$. *Images are at times* $t = 0, 105, 210, 315\,s$. *See second and third examples in supplemental movie* 3.

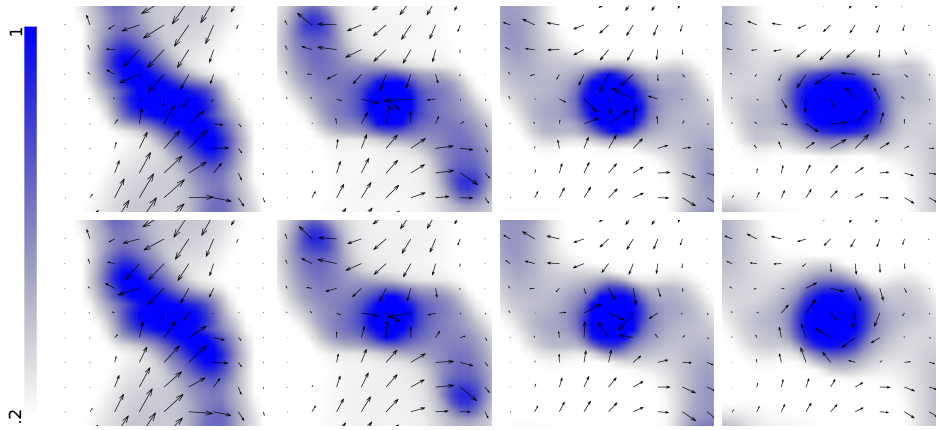

FIG. 13. *Magnified view of vortex ring experiment with evolved motor model (top row) and simplified motor model (bottom row),* $U_r = 0$ *and* $V_{sp} = 0$. *A counterclockwise velocity field forms with the evolved motor model, whereas a clockwise velocity field forms with the simplified motor model. Images are at times* $t = 150, 300, 450, 600\,s$.

but also changes the flow features that emerge over time. We observe that for the highest tested value, $C = 250$, any cell with a $\Psi_{spatial,z_0}$ value over a threshold results in fully bound motors, exercising the second argument to the minimum function in the definition of the simplified motor model (SM). Therefore two cells with distinct $\Psi_{spatial,z_0}$ values above the threshold will produce motor forces of equal magnitude, changing the emergent behavior within the assay.

Perturbation with and without motor-based fluid forces. In Figure 15 (and supplemental movie 5), we repeat the perturbation experiment with self-propulsion in the presence and absence of the hydrodynamic forces generated by the motor proteins. This allows us to test the observation of [29] that the stability and size of the observed filament patterns depend on long-range hydrodynamic interactions. Consistent with

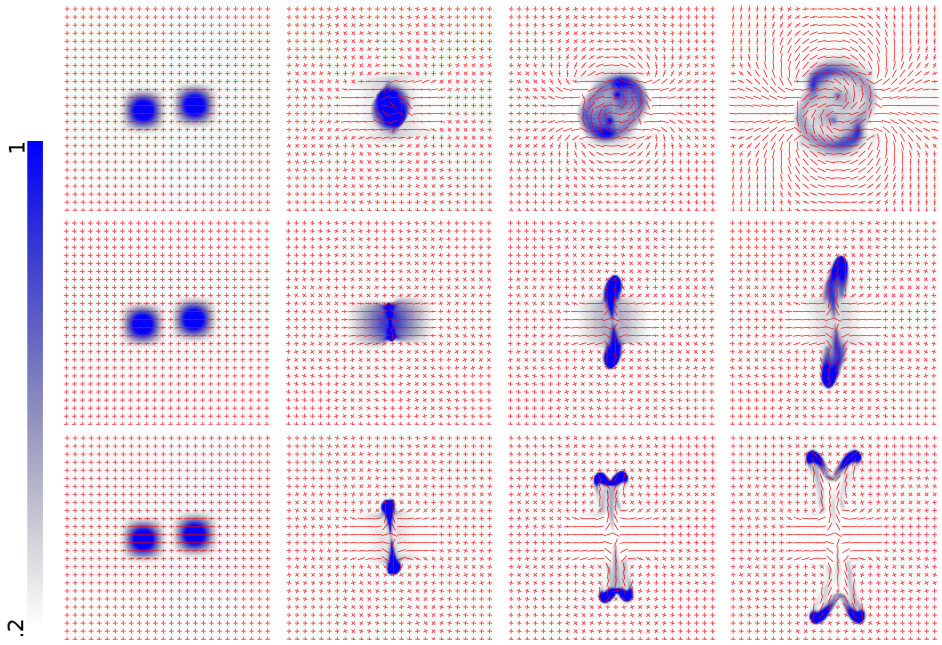

FIG. 14. *Antiparallel colliding clump experiment with simplified motor model,* $U_r = .001$ *and* $V_{sp} = 0$. *First row:* $C = 10$. *Second row:* $C = 50$. *Third row:* $C = 250$. *First row images are at times* $t = 0, 300, 600, 900\,s$. *Second row images are at times* $t = 0, 21, 42, 63\,s$. *Third row images are at times* $t = 0, 15, 30, 45\,s$. *See supplemental movie* 4.

[29], we observe larger flow structures forming in a shorter amount of time in the presence of the fluid flows driven by the motor proteins. We used the simplified motor model, $C = 100$, $U_r = .01$, and $V_{\text{sp}} = .1$.

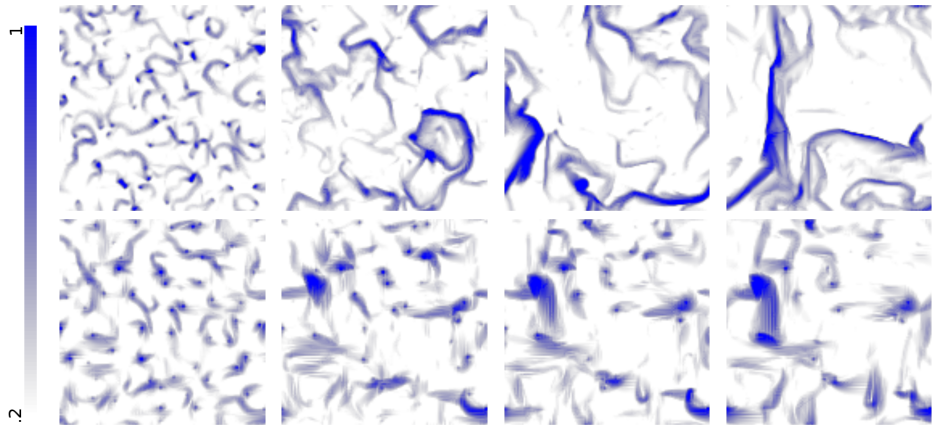

FIG. 15. *Perturbation experiment with (first row) and without (second row) motor-based fluid forces, showing faster formation of larger-scale features in the former case. First row images are at times* $t = 150, 300, 450, 600\,s$. *Second row images are at times* $t = 300, 600, 900, 1200\,s$. *See supplemental movie* 5.

5. Conclusions. We have developed a modeling and simulation framework coupling multiple microscopic models of propulsion to macroscopic steric and hydrodynamic interactions in a quasi–two-dimensional assay. Populations of bound and free motor proteins and microtubules are represented as continuum distributions. The framework facilitates study of the relative effects of hydrodynamic and steric interactions on emergent phenomena. Stress tensors arising from rotational and translational steric interactions and self-propulsion are supported in addition to body forces from active motor proteins. Experimentation is needed to empirically determine the steric interaction parameters U_r and U_x. We avoid closure approximations in the z-dimension, and high precision around a z-plane of interest is achieved without incurring significant computational overhead. Results demonstrate our framework's ability to replicate some of the behavior of individual and colliding clumps of filaments, including crossovers, alignment, merging, and splitting [30], and thus support observations of [29] regarding hydrodynamic effects.

We present two motor protein models, the evolved motor model, which incorporates motor head procession and binding/unbinding dynamics, and the simplified motor model, which determines the bound motor distribution instantaneously as a function of the microtubule distribution and therefore eliminates the high-dimensional and computationally expensive motor evolution at the smaller timescale t^*. While the different models may yield visually similar motor distributions, they can result in qualitatively different dynamics, as illustrated in Figure 13. Additional motor models could be investigated within our framework, for example, models accounting for cooperativity or competition between motor proteins.

One limitation of our model is the way we model the motor stalk force. The motor stalk force has a component parallel to the filament, perpendicular to the filament and in the x, y-plane, and in the z-direction. The component parallel to the filament is equivalent to the motor force we apply. We ignore the perpendicular component in the x, y-plane, which would act to translate and reorient the filament to align the filament director with the in-plane motor stalk force. We also ignore the component in the z-direction, which would act to move filaments in the z-direction, since we phenomenologically model the filament distribution in the z-direction. In future work it would be interesting to refine our motor model to capture the second component of the force as well.

Our model applies to a microtubule gliding assay, where the motors generate force monopoles. If multiheaded motor complexes bind two filaments, this leads to force dipoles as in [10]. While our framework could be extended to such cases, in practice this leads to a very high-dimensional motor complex state space which may require additional work to make it feasible.

Motor forces on the fluid compose flow features in the microtubule density by advecting all local microtubules with the same velocity. Even without any steric interaction terms, two colliding clumps will proceed in a direction roughly equal to the average of their orientations. However, the motor forces acting on the fluid are prone to cancellation in isotropic or antialigned microtubule configurations. Combining either motor model with a self-propulsion term in the microtubule advective flux provides a mechanism for antiparallel sliding, resulting in persistent motion of the microtubules. Addition of the self-propulsion term enables the passthrough of colliding clumps, consistent with the simulations of [30].

REFERENCES

[1] I. S. Aranson and L. S. Tsimring, *Pattern formation of microtubules and motors: Inelastic interaction of polar rods*, Phys. Rev. E, 71 (2005), 050901, https://doi.org/10.1103/PhysRevE.71.050901.

[2] A. Baskaran and M. C. Marchetti, *Hydrodynamics of self-propelled hard rods*, Phys. Rev. E, 77 (2008), 011920.

[3] G. K. Batchelor, *The stress system in a suspension of force-free particles*, J. Fluid Mech., 41 (1970), pp. 545–570, https://doi.org/10.1017/S0022112070000745.

[4] R. B. Bird, C. F. Curtiss, R. C. Armstrong, and O. Hassager, *Dynamics of Polymeric Liquids, Vol.* 2: *Kinetic Theory*, 2nd ed., Wiley-Interscience, Hoboken, NJ, 1987.

[5] M. Doi and S. F. Edwards, *The Theory of Polymer Dynamics*, Oxford University Press, Oxford, UK, 1986.

[6] K. Drescher, R. E. Goldstein, N. Michel, M. Polin, and I. Tuval, *Direct measurement of the flow field around swimming microorganisms*, Phys. Rev. Lett., 105 (2010), 168101.

[7] C. Dullemond, *Lecture on Numerical Fluid Dynamics*, http://www.mpia-hd.mpg.de/~dullemon/lectures/fluiddynamics08, 2008.

[8] B. Ezhilan, M. J. Shelley, and D. Saintillan, *Instabilities and nonlinear dynamics of concentrated active suspensions*, Phys. Fluids, 25 (2013), 070607.

[9] M. Frigo and S. G. Johnson, *FFTW: An adaptive software architecture for the FFT*, in Proceedings of the 1998 IEEE International Conference on Acoustics, Speech and Signal Processing, vol. 3, 1998, pp. 1381–1384, https://doi.org/10.1109/ICASSP.1998.681704.

[10] T. Gao, R. Blackwell, M. A. Glaser, M. Betterton, and M. J. Shelley, *Multiscale modeling and simulation of microtubule–motor-protein assemblies*, Phys. Rev. E, 92 (2015), 062709.

[11] L. Giomi, L. Mahadevan, B. Chakraborty, and M. F. Hagan, *Excitable patterns in active nematics*, Phys. Rev. Lett., 106 (2011), 218101, https://doi.org/10.1103/PhysRevLett.106.218101.

[12] C. Hohenegger, S. Cook, and T. Shinar, *Dimensional reduction of a multiscale continuum model of microtubule gliding assays*, SIAM J. Appl. Math., 74 (2014), pp. 1338–1353, https://doi.org/10.1137/140961535.

[13] C. Hohenegger and M. J. Shelley, *Dynamics of complex biofluids*, in New Trends in the Physics and Mechanics of Biological Systems, M. Ben Amar, A. Goriely, M. M. Müller, and L. F. Cugliandolo, eds., Ecole de Physique des Houches Session XCII, 2009, Oxford University Press, Oxford, UK, 2011, Chapter 3, pp. 65–92.

[14] J. Howard, *The movement of kinesin along microtubules*, Annu. Rev. Physiol., 58 (1996), pp. 703–729.

[15] J. Kierfeld, K. Frentzel, P. Kraikivski, and R. Lipowsky, *Active dynamics of filaments in motility assays*, European Phys. J., 157 (2008), pp. 123–133.

[16] P. Kraikivski, R. Lipowsky, and J. Kierfeld, *Enhanced ordering of interacting filaments by molecular motors*, Phys. Rev. Lett., 96 (2006), 258103, https://doi.org/10.1103/PhysRevLett.96.258103.

[17] H. Y. Lee and M. Kardar, *Macroscopic equations for pattern formation in mixtures of microtubules and molecular motors*, Phys. Rev. E, 64 (2001), 056113, https://doi.org/10.1103/PhysRevE.64.056113.

[18] T. B. Liverpool, *Active gels: Where polymer physics meets cytoskeletal dynamics*, Philos. Trans. Roy. Soc. London A, 364 (2006), pp. 3335–3355.

[19] T. B. Liverpool and M. C. Marchetti, *Bridging the microscopic and the hydrodynamic in active filament solutions*, Europhys. Lett., 69 (2005), pp. 846–852, https://doi.org/10.1209/epl/i2004-10414-0.

[20] F. Nédélec, *Computer simulations reveal motor properties generating stable antiparallel microtubule interactions*, J. Cell Biol., 158 (2002), pp. 1005–1015, https://doi.org/10.1083/jcb.200202051.

[21] F. Nédélec and D. Foethke, *Collective Langevin dynamics of flexible cytoskeletal fibers*, New J. Phys., 9 (2007), 427, https://doi.org/10.1088/1367-2630/9/11/427.

[22] F. Nédélec, T. Surrey, and A. C. Maggs, *Dynamic concentration of motors in microtubule arrays*, Phys. Rev. Lett., 86 (2001), pp. 3192–3195, https://doi.org/10.1103/PhysRevLett.86.3192.

[23] F. J. Nédélec and T. Surrey, *Dynamics of microtubule aster formation by motor complexes*, C. R. Acad. Sci. Paris, 4 (2001), pp. 841–847.

[24] C. Peskin, *The immersed boundary method*, Acta Numer., 11 (2002), pp. 479–517, https://doi.org/10.1017/S0962492902000077.

[25] S. L. Rogers and J. M. Scholey, *Motility assays for microtubule motor proteins*, Nature Encycloped. Life Sci. (eLS), 2004, https://doi.org/10.1038/npg.els.0002621.

[26] D. Saintillan and M. J. Shelley, *Instabilities and pattern formation in active particle suspensions: Kinetic theory and continuum simulations*, Phys. Rev. Lett., 100 (2008), 178103, https://doi.org/10.1103/PhysRevLett.100.178103.

[27] D. Saintillan and M. J. Shelley, *Instabilities, pattern formation, and mixing in active suspensions*, Phys. Fluids, 20 (2008), 123304, https://doi.org/10.1063/1.3041776.

[28] S. Sankararaman, G. I. Menon, and P. B. Sunil Kumar, *Self-organized pattern formation in motor-microtubule mixtures*, Phys. Rev. E, 70 (2004), 031905, https://doi.org/10.1103/PhysRevE.70.031905.

[29] V. Schaller, C. Weber, E. Frey, and A. R. Bausch, *Polar pattern formation: Hydrodynamic coupling of driven filaments*, Soft Matter, 7 (2011), pp. 3213–3218, https://doi.org/10.1039/C0SM01063D.

[30] V. Schaller, C. Weber, C. Semmrich, W. Frey, and A. R. Bausch, *Polar patterns of driven filaments*, Nature, 467 (2010), pp. 73–77, https://doi.org/10.1038/nature09312.

[31] M. J. Shelley, *The dynamics of microtubule/motor-protein assemblies in biology and physics*, Annu. Rev. Fluid Mech., 48 (2016), pp. 487–506.

[32] T. Shinar, M. Mana, F. Piano, and M. J. Shelley, *A model of cytoplasmically driven microtubule-based motion in the single-celled* caenorhabditis elegans *embryo*, Proc. Natl. Acad. Sci. USA, 108 (2011), pp. 10508–10513.

[33] Y. Sumino, K. H. Nagai, Y. Shitaka, D. Tanaka, K. Yoshikawa, H. Chaté, and K. Oiwa, *Large-scale vortex lattice emerging from collectively moving microtubules*, Nature, 483 (2012), pp. 448–452, https://doi.org/10.1038/nature10874.

[34] S. Swaminathan, F. Ziebert, D. Karpeev, and I. S. Aranson, *Motor-mediated alignment of microtubules in semidilute mixtures*, Phys. Rev. E, 79 (2009), 036207, https://doi.org/10.1103/PhysRevE.79.036207.

[35] Q. Wang, *A hydrodynamic theory for solutions of nonhomogeneous nematic liquid crystalline polymers of different configurations*, J. Chem. Phys., 116 (2002), pp. 9120–9136.